Tmbim5 loss causes muscle atrophy in zebrafish without exacerbating mcu or slc8b1 knockout phenotypes

Iga Wasilewska[1,4#], Łukasz Majewski[2], Dobrochna Adamek-Urbańska[3], Sofiia Baranykova[2], Matylda Macias[2], Aleksandra Szybińska[2] and Axel Methner[4#]

Running title: TMBIM5 Fish

[1]Mossakowski Medical Research Institute, Polish Academy of Sciences, 5 Pawinskiego Str., 02-106 Warsaw, Poland

[2]International Institute of Molecular and Cell Biology in Warsaw, 4 Ks. Trojdena Str., 02-109 Warsaw, Poland

[2]Department of Ichthyology and Biotechnology in Aquaculture, Institute of Animal Sciences, Warsaw University of Life Sciences, Ciszewskiego 8 St., 02-786 Warsaw, Poland

[4]University Medical Center of the Johannes Gutenberg-University Mainz, Institute for Molecular Medicine, Langenbeckstr. 1, D-55131 Mainz, Germany.

[#]Correspondence should be addressed to: Axel Methner MD, University Medical Center of the Johannes Gutenberg-University Mainz, Institute for Molecular Medicine, Langenbeckstr. 1, D-55131 Mainz, Germany, Tel.: +49-6131-17-2695, Email: axel.methner@gmail.com or to Iga Wasilewska, Mossakowski Medical Research Institute, Polish Academy of Sciences, 5 Pawinskiego Str., 02-106 Warsaw, Poland, Email: iwasilewska@imdik.pan.pl

The final character count: 90552

Abstract

Mitochondria generate ATP by establishing a proton gradient across the inner membrane, which also drives calcium uptake via the mitochondrial calcium uniporter (MCU), while sodium-dependent NCLX (encoded by *SLC8B1*) facilitates efflux. The absence of severe phenotypes in *MCU*-knockout models suggests redundant calcium transport mechanisms. We investigated the role of TMBIM5, a potential bidirectional mitochondrial calcium transporter, by generating zebrafish lacking Tmbim5, Slc8b1, or both. *tmbim5*-knockout fish exhibited growth impairment, muscle atrophy (particularly in slow-twitch fibers), increased brain cell death, and reduced mitochondrial membrane potential without altering steady-state mitochondrial calcium levels. *slc8b1*-deficient fish demonstrated significantly attenuated sodium-dependent calcium efflux and increased larval mortality but were otherwise normal. Surprisingly, *tmbim5*/*mcu* and *tmbim5*/*slc8b1* double knockouts were viable with normal Mendelian distribution. *tmbim5*/*slc8b1* double knockouts displayed impaired mitochondrial calcium uptake capacity, diminished calcium efflux, and severely disrupted cristae architecture not observed in single knockouts. These findings suggest that Tmbim5 functions predominantly in mitochondrial calcium efflux rather than influx and indicate that robust compensatory mechanisms maintain mitochondrial calcium homeostasis despite disruption of these transport pathways.

Key words (5, alphabetical): *In vivo* Ca^{2+} measurements / Ion fluxes / Mcu / Nclx / Tmbim5 /

Introduction

Mitochondria generate ATP by harnessing a proton and electron gradient generated by the electron transport system. The negative mitochondrial membrane potential across the inner mitochondrial membrane also acts as the driving force for the uptake of the universal cellular messenger calcium (Ca^{2+}). Increased mitochondrial Ca^{2+} levels enhance oxidative phosphorylation, which leads to increased ATP production. Mitochondria also serve as cellular Ca^{2+} sinks, making mitochondrial Ca^{2+} uptake important for cellular Ca^{2+} signaling in general. Therefore mitochondrial Ca^{2+} homeostasis is a finely tuned process that involves the coordinated action of Ca^{2+} transporters, regulatory proteins, and interactions with the endoplasmic reticulum (ER).

The mechanisms governing mitochondrial Ca^{2+} transport are not fully understood. The mitochondrial Ca^{2+} channel mediating inward Ca^{2+} flux is the mitochondrial Ca^{2+} uniporter (MCU) (Baughman *et al*, 2011; De Stefani *et al*, 2011) which is part of a large protein complex which contains several MCU-interacting and regulatory proteins like MICU1 (mitochondrial uptake 1) (Mallilankaraman *et al*, 2012b), MICU2 (Patron *et al*, 2014), EMRE (essential MCU regulator) (Vais *et al*, 2016) and MCUR1 (mitochondrial Ca^{2+} uniporter regulator 1) (Vais *et al*, 2015; Mallilankaraman *et al*, 2012a). *Mcu* knockout (KO) in mice leads to mild phenotypes in a CD1 background (Pan *et al*, 2013) but embryonic lethality in C57Bl/6 (Murphy *et al*, 2014). In zebrafish, *mcu* knockdown did not alter survival or activity in zebrafish larvae (Soman *et al*, 2017). Also *mcu* KO had no effect on viability, fertility, morphology or swimming behavior in zebrafish although it abolished mitochondrial Ca^{2+} uptake similar to the well-characterized MCU inhibiting compound ruthenium red (RuR) (Soman *et al*, 2019a; Tomar *et al*, 2019; Langenbacher *et al*, 2020). However, *in vivo* studies in zebrafish photoreceptors suggest alternative Ca^{2+} entry pathways that can compensate for Mcu loss (Bisbach *et al*, 2020). One disputed candidate is Leucine Zipper And EF-Hand Containing Transmembrane Protein 1 (LETM1), identified by a genome-wide screen as a RuR-sensitive mitochondrial Ca^{2+}/H^{+}-antiporter (Jiang *et al*, 2009). Originally, LETM1 was described as part of the mitochondrial K^{+}/H^{+} exchanger (Nowikovsky *et al*, 2004). Ca^{2+} efflux is primarily mediated by the Na^{+}/Ca^{2+} exchanger NCLX (Palty *et al*, 2010), whose knockout causes embryonic lethality in mice (Luongo *et al*, 2017). Recent evidence suggests that also Transmembrane Protein 65 (TMEM65) is involved in Na^{+}-dependent Ca^{2+} efflux from mitochondria (Vetralla *et al*, 2023; Zhang *et al*, 2023) and may act as a positive regulator of NCLX (Garbincius *et al*, 2023). Another mitochondrial Ca^{2+} extrusion system is the mitochondrial permeability transition pore (mPTP), a non-selective high-conductance pore of debated identity (Bernardi *et al*, 2023; Altschuld *et al*, 1992). High mitochondrial Ca^{2+} concentrations lead to opening of the mPTP which, when sustained, causes mitochondrial swelling, breakdown of mitochondrial membrane potential, and eventually cell death (reviewed in (Orrenius *et al*, 2015)).

Recently, a novel candidate for mitochondrial Ca^{2+} transport emerged, the transmembrane BAX inhibitor motif containing protein 5 (TMBIM5) initially linked to the regulation of mitochondrial morphology, as loss of TMBIM5 in cells resulted in mitochondrial fragmentation and a disrupted cristae structure (Oka *et al*, 2008; Seitaj *et al*, 2020; Zhang *et al*, 2022; Austin *et al*, 2022). Loss of TMBIM5 was also observed to increase the sensitivity of cells to apoptosis (Oka *et al*, 2008; Seitaj *et al*, 2020; Patron *et al*, 2022). In *vivo*, mice genetically engineered with a specific alteration (D326R) that presumably disrupts the channel pore of the TMBIM5 protein (Bultynck *et al*, 2014) and leads to degradation of the protein (Zhang *et al*, 2022) exhibit several significant physiological and structural changes. These mice show a higher mortality during embryonic development or shortly after birth and develop a skeletal myopathy characterized by reduced muscle strength. These observations

were closely linked to several mitochondrial abnormalities most dramatically obvious in mitochondria obtained from skeletal muscle. This included a disrupted cristae structure, premature mPTP opening, decreased ability of mitochondria to take up Ca^{2+}, and swollen mitochondria (Zhang *et al*, 2022).

Two studies demonstrated that TMBIM5, when reconstituted in liposomes, can act as a Ca^{2+} transporter in the presence of a pH gradient (Patron *et al*, 2022; Austin *et al*, 2022). Inhibiting NCLX-mediated mitochondrial Ca^{2+} efflux by CGP-37157 (CGP) (Austin *et al*, 2022) or *NCLX* knockdown (Patron *et al*, 2022) resulted in a diminished mitochondrial Ca^{2+} retention capacity in *TMBIM5* KO in human embryonic kidney (HEK) cells and reduced RuR-induced mitochondrial Ca^{2+} efflux (Austin *et al*, 2022). *TMBIM5* KO cells also accumulated more matrix Ca^{2+} upon ER Ca^{2+} release mediated by inhibition of the sarco/endoplasmic ATPase (SERCA) with thapsigargin (Patron *et al*, 2022) or stimulation of inositol trisphosphate receptor-mediated Ca^{2+} release with ATP or carbachol (Austin *et al*, 2022). Concurrent knockout of *MCU* rescued elevated apoptosis induced by staurosporine in *TMBIM5*$^{-/-}$ cells (Patron *et al*, 2022), suggesting that TMBIM5 can mediate Ca^{2+} extrusion from mitochondria and that its function at least partially overlaps with NCLX. Zhang et al., in contrast, found that TMBIM5 overexpression in HEK cells enhanced mitochondrial Ca^{2+} uptake following ER Ca^{2+} release (Zhang *et al*, 2022), suggesting that TMBIM5 may operate bidirectionally under certain conditions. This study also demonstrated that under steady-state conditions, loss of TMBIM5 results in increased potassium and reduced proton levels in the mitochondrial matrix suggesting a broader role in mitochondrial ion exchange (Zhang *et al*, 2022) in line with a potential interaction of TMBIM5 with LETM1 (Austin *et al*, 2022). The physiological significance of these mechanisms *in vivo*, especially the crosstalk of TMBIM5 with MCU and NCLX, is unclear.

Due to their translucency, zebrafish are an ideal tool to study mitochondrial Ca^{2+} dynamics *in vivo* (Kettunen, 2020; Mandal *et al*, 2018). In the present study, we generated *tmbim5* and *slc8b1* KO fish by CRISPR/Cas9-mediated gene editing (Gasanov *et al*, 2021) and observed that loss of Tmbim5 results in a muscle phenotype associated with delayed hatching, smaller size, and increased cell death in the brain while loss of Slc8b1 resulted in increased larvae mortality. In living larvae, Tmbim5 depletion did not affect mitochondrial Ca^{2+} levels. To investigate potential interactions with known Ca^{2+} transport systems, we generated *tmbim5*/*mcu* and *tmbim5*/*slc8b1* double knockouts. Both lines were viable without major phenotypes, however, *tmbim5*/*slc8b1* double knockouts exhibited reduced mitochondrial Ca^{2+} uptake and sodium-dependent Ca^{2+} extrusion together with a pathological cristae architecture. The mild phenotypes of double knockouts indicate either strong compensatory mechanisms or that additional Ca^{2+} transport pathways maintain mitochondrial Ca^{2+} homeostasis in the absence of these proteins.

Results

Tmbim5-deficient larvae are smaller and exhibit a reduced hatching efficiency

The zebrafish genome contains only one *TMBIM5* orthologue which is expressed as early as six hours post fertilization (hpf) and plateaus after 24 hours (Fig. 1A). To study the effect of Tmbim5 deficiency, we generated mutant fish by introducing a deletion in exon 4 using CRISPR/Cas9 genome editing (Gasanov *et al*, 2021). This resulted in a profound decrease in *tmbim5* mRNA (Fig. 1B); mutants (*tmbim5*$^{-/-}$) reached adulthood and the Mendelian distribution was unchanged (Fig. 1C). Mutant larvae took longer to hatch than wild-type (WT, *tmbim5*$^{+/+}$) controls (Fig. 1D) and this correlated with reduced tail coiling (Fig. 1E), spontaneous movements of the tail that enable the embryo to escape from its chorion (Lessman & Carver, 2014). This suggested a possible reduction in muscle strength as also

observed in mice with a channel pore mutation in TMBIM5 (Zhang *et al*, 2022). Despite that, mutant larvae displayed unchanged spontaneous locomotor activity in an open field test (Fig. EV1A) as well as after stimulating mobility in a visual-motor response test (Fig. EV1B). Tmbim5-deficient larvae were morphologically normal (Fig. 1F) but shorter, had a smaller eye diameter and thinner somites (Fig. 1G). This reduction in somite thickness was not solely attributable to the overall reduction in whole-body size, as the ratio of somite thickness to whole-body length was also decreased in *tmbim5*$^{-/-}$ larvae (Fig. 1G). Together these results suggest a role for Tmbim5 in body size and muscle strength.

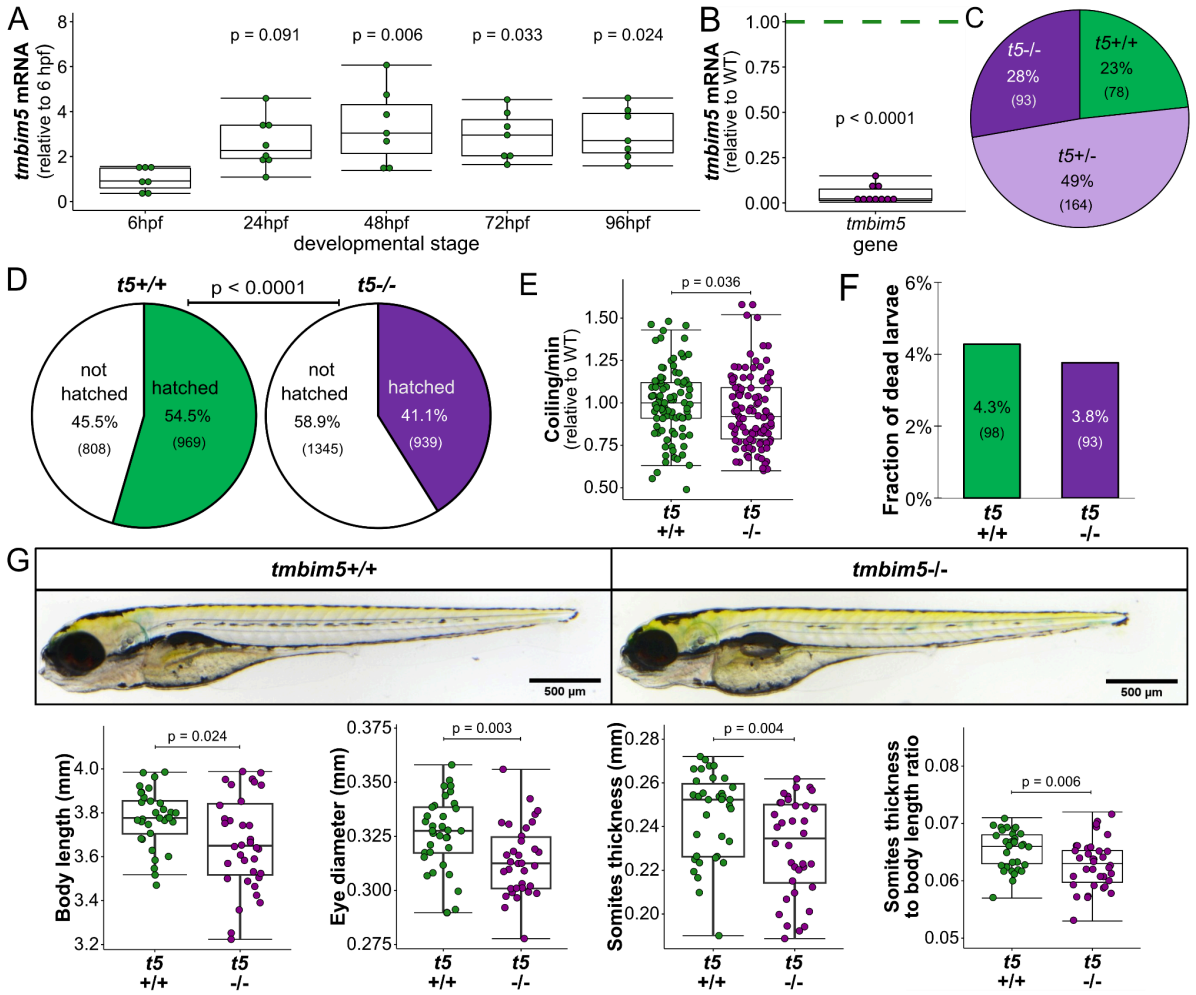

Figure 1. Tmbim5-deficient larvae are smaller and exhibit a reduced hatching efficiency

A) *tmbim5* mRNA levels at different developmental stages, measured using quantitative PCR (qPCR). Expression was normalized to 6 hours post-fertilization (hpf), with *18S* used as a reference gene. Data are presented as box-and-whisker plots, where the box represents the 25th–75th percentile, and the whiskers indicate the minimum and maximum values. Each dot represents an independent biological replicate (n = 7–8; each RNA sample was isolated from 30 embryos/larvae). Number of experiments = 4. Statistical analysis: one-way ANOVA followed by Tukey's HSD test; p-values indicate comparisons with 6 hpf.

B) Decreased *tmbim5* mRNA levels in 5 days post-fertilization (dpf) *tmbim5*$^{-/-}$ larvae, quantified using qPCR and normalized to WT levels. *rpl13a* and *ef1a* were used as reference genes. Data are shown as box-and-whisker plots, with the box representing the 25th–75th percentile and the whiskers indicating the minimum and maximum values. Each dot represents an independent biological replicate (n = 10; each RNA sample was isolated from 30 larvae). Number of experiments = 5. Statistical analysis: one-sample t-test.

C) Genotype distribution of offspring from *tmbim5* (*t5*)$^{+/-}$ zebrafish breeding does not deviate from expected Mendelian ratios (n indicated in brackets). Number of experiments = 4. Statistical analysis: Chi-square test.

D) Reduced hatching efficiency of *tmbim5*$^{-/-}$ larvae. n is indicated in brackets. Number of experiments = 6. Statistical analysis: Chi-square test.

E) Decreased coiling activity of *tmbim5*$^{-/-}$ embryos at 1 dpf. The mean number of coiling movements per minute, normalized to WT from the same experiment, is shown as box-and-whisker plots (box: 25th–75th percentile; whiskers: min to max). Each dot represents an individual embryo (*n* = 94–104). Number of experiments = 6. Statistical analysis: one-sample Wilcoxon test.

F) Survival of *tmbim5*$^{-/-}$ larvae up to 5 dpf is not significantly affected. *n* is indicated in brackets. Number of experiments = 7. Statistical analysis: Chi-square test.

G) Abnormal morphology of *tmbim5*$^{-/-}$ larvae at 5 dpf. Representative images of WT (*tmbim5*$^{+/+}$) and *tmbim5*$^{-/-}$ larvae are shown. Morphometric analysis results are presented as box-and-whisker plots (box: 25th–75th percentile; whiskers: min to max), with each dot representing an individual larva (*n* = 34–36). Number of experiments = 3. Statistical analysis: Mann–Whitney test (for body length and somite thickness) or *t*-test.

Adult Tmbim5-deficient fish weigh less and show signs of muscle atrophy most pronounced in slow twitch muscle fibers

We next studied the effects of Tmbim5 deficiency in adult zebrafish. Similar to larvae, *tmbim5*$^{-/-}$ adult fish had a normal morphology, a tendency to be smaller and a significant reduction in weight compared to WT fish (Fig. 2A). Locomotor activity of adult fish was unchanged (Fig. EV1C). Similar to mouse TMBIM5, zebrafish Tmbim5 is expressed in most tissues with the highest mRNA expression levels in brain and muscle (Fig. 2B). A histopathological examination of these tissues and liver revealed no major differences (Fig. EV2A-J).

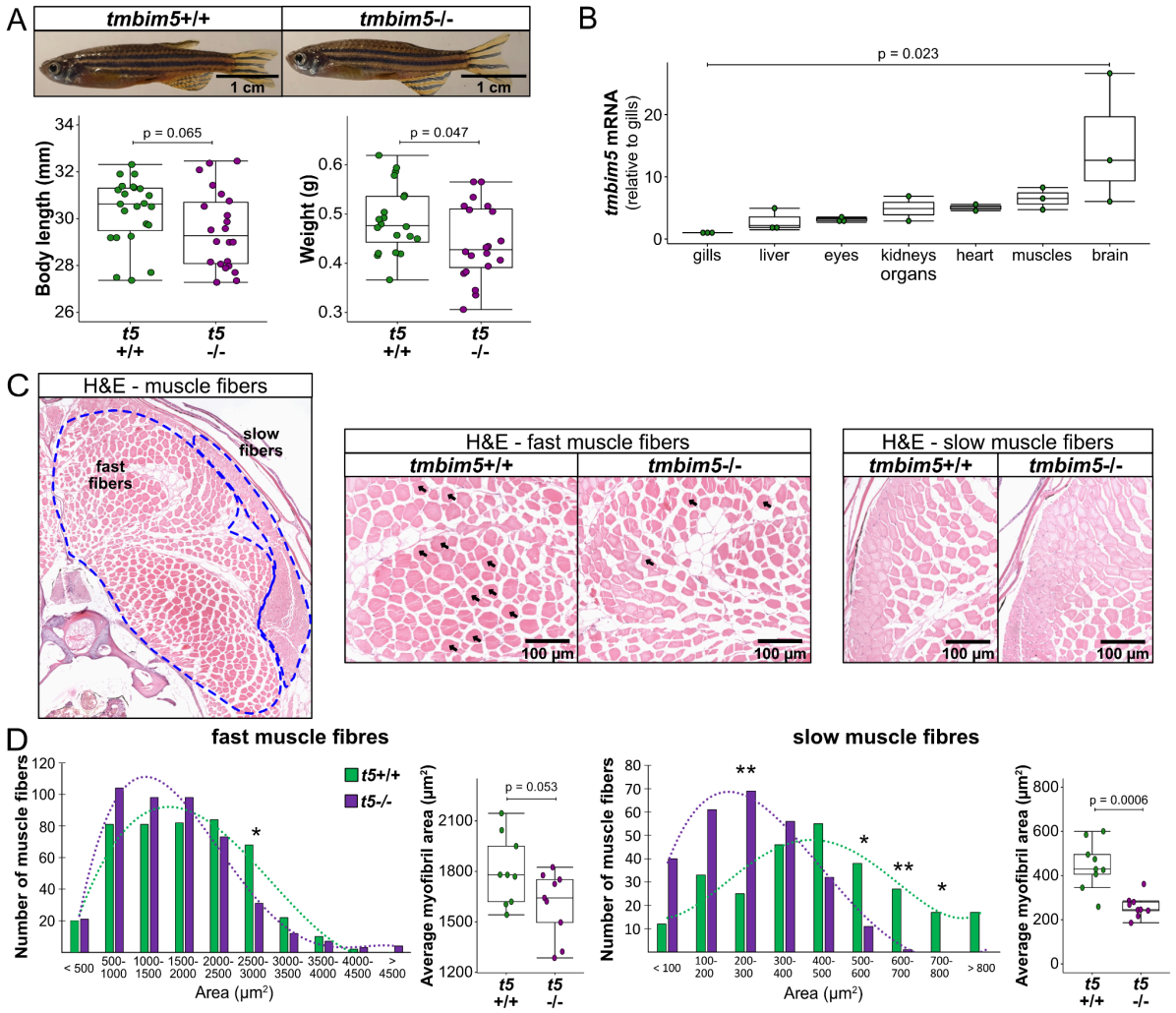

Figure 2. Adult Tmbim5-deficient fish weigh less and show signs of muscle atrophy most pronounced in slow twitch muscle fibers

A) Smaller size of *tmbim5*$^{-/-}$ adult fish. Representative images of WT and *tmbim5*$^{-/-}$ 8-month-old zebrafish. Morphometric analysis results are presented as box-and-whisker plots (box: 25th–75th percentile; whiskers: min to max), with each dot

representing an individual fish (n = 19–23). Number of experiments = 3 (weight) or 4 (body length). Statistical analysis: Mann–Whitney test (body length) or *t*-test (weight).

B) *tmbim5* mRNA levels in various adult zebrafish organs measured using qPCR. Expression was normalized to the gills (the organ with the lowest *tmbim5* expression), with *rpl13a* used as a reference gene. Data are presented as box-and-whisker plots (box: 25th–75th percentile; whiskers: min to max), with each dot representing an independent biological replicate (n = 2–3; each RNA sample was isolated from 2 fish). Number of experiments = 3. Statistical analysis: Kruskal-Wallis test followed by Dunn's test.

C) Representative images of hematoxylin and eosin (H&E)-stained skeletal muscle sections from adult (8-month-old) zebrafish with fast- and slow-twitch fibers indicated. Middle panel: magnification of the area with fast fibers images from WT and *tmbim5*$^{-/-}$. Arrows indicate fibers of 2500-3000 µm², which are significantly reduced in number in the mutants. Right panel: magnification of the area with slow-twitch fibers images of WT and *tmbim5*$^{-/-}$.

D) Smaller cross-sectional area of fast and slow muscle fibers in *tmbim5*$^{-/-}$ adult fish. Histograms showing the distribution of fast (left panel) and slow (right panel) muscle fiber cross-sectional areas in WT and *tmbim5*$^{-/-}$ fish. The mutant distribution is shifted toward smaller fibers. Statistical analysis: Chi-square test (p = 0.0009). Differences in the number of fibers of specific sizes are marked with an asterisk (* $p < 0.05$), analyzed using the Mann–Whitney test or *t*-test with Benjamini-Hochberg (BH) correction for multiple comparisons. Box-and-whisker plots (box: 25th–75th percentile; whiskers: min to max) showing the trend toward a reduction in the average myofibril area in mutants. Each dot represents the average for one section (50 fibers analyzed per section, n = 9). Number of fish = 3. Statistical analysis: *t*-test.

We then analyzed the skeletal muscle in more detail. In zebrafish slow (red) and fast (white) twitch fibers are segregated, allowing analysis without immunohistochemical staining (Hasumura & Meguro, 2016) (Fig. 2C). Slow twitch fibers are rich in mitochondria and depend more on aerobic metabolism than fast (white) twitch muscle fibers (Control of muscle fibre-type diversity during embryonic development: The zebrafish paradigm, 2013). A morphometric analysis of these fibers demonstrated a shift towards smaller fibers, a decline in the fibers with a cross-sectional area of 2500-3000 µm^2, and a reduction in the average cross-sectional area in mutant fish. All of these changes were more pronounced in slow twitch muscle fibers than in fast twitch fibers (Fig. 2D). The more pronounced atrophy of small muscle fibers probably reflects a mitochondrial dysfunction and is in line with the reduced muscle strength observed in larvae.

Live imaging reveals unchanged mitochondrial Ca^{2+} levels in the brain of Tmbim5-deficient fish

To clarify whether changes in the mitochondrial Ca^{2+} homeostasis could explain the effects of Tmbim5 deficiency, we took advantage of the translucency of zebrafish larvae which allows the quantification of (mitochondrial) Ca^{2+} levels in the living animal using genetically-encoded Ca^{2+} sensors. We chose the hindbrain because *tmbim5* is strongly expressed there as shown by whole-mount in situ hybridization (Fig. 3A); importantly no staining was observed in *tmbim5*$^{-/-}$ larvae proving the specificity of the riboprobe. We also found increased cell death in this tissue as demonstrated by staining the brain of *tmbim5*$^{-/-}$ larvae with Acridine Orange (Fig. 3B) implying functional changes associated with Tmbim5 deficiency. We crossed *tmbim5* mutant with fish *Tg*(*CEPIA2mt*) expressing the mitochondrially targeted sensor CEPIA2mt (Suzuki *et al*, 2014) under the neuronal promoter *HuC*/*elavl3* (*ELAV like neuron-specific RNA binding protein 3*) and imaged mitochondria in the optic tectum, a dorsally located part of the hindbrain which is accessible for imaging in *tmbim5*$^{-/-}$;*Tg*(*CEPIA2mt*) and *tmbim5*$^{+/+}$;*Tg*(*CEPIA2mt*) larvae (Fig. 3A', Fig. 3C). We tried to measure baseline fluorescence and found no significant differences between *tmbim5*$^{-/-}$ and *tmbim5*$^{+/+}$, but a very large variance within groups making it impossible to quantify steady-state mitochondrial Ca^{2+} levels using this probe (Fig. 3D). It is noteworthy that CEPIA2mt is not a ratiometric probe (Suzuki *et al*, 2014) and therefore does not provide the best possible quantification of basal Ca^{2+} levels.

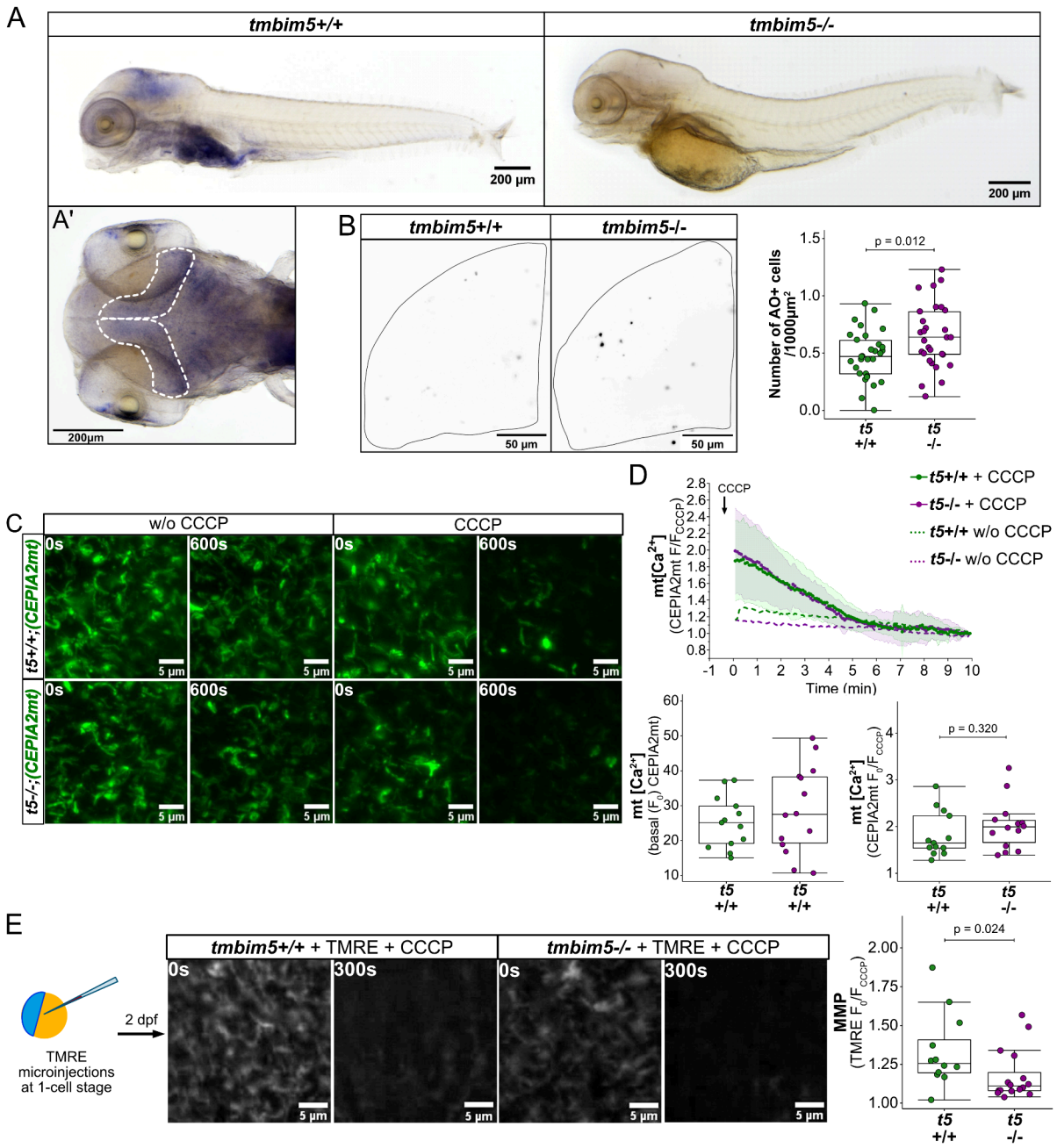

Figure 3. Live imaging reveals unchanged mitochondrial Ca^{2+} levels in the brain of Tmbim5-deficient fish

A) *tmbim5* transcript detected using whole-mount in situ hybridization in 4 dpf wild-type (WT) larvae, with a complete loss of expression in *tmbim5*$^{-/-}$ larvae. A' Dorsal view of the optic tectum region outlined with a dashed line. Number of experiments = 4.

B) Increased cell death in the optic tectum of *tmbim5-/-* larvae detected using Acridine Orange (AO) staining. Representative images of WT and *tmbim5*$^{-/-}$ larvae (black dots indicate high AO signals). Quantification results are presented as box-and-whisker plots (box: 25th–75th percentile; whiskers: min to max), with each dot representing an individual larva (*n* = 29–30, number of experiments = 3). Statistical analysis: *t*-test.

C-D) No alteration in basal mtCEPIA2 signal intensity or mitochondrial Ca^{2+} response to depolarization with CCCP. CCCP (10 µM) was used to depolarize mitochondria, and the F_0/F_{CCCP} ratio was calculated. Larvae incubated in E3 medium without CCCP (w/o CCCP) served as negative controls. C) Representative images of the region of interest (ROI) at the beginning and after 10 min of CCCP treatment. D) Upper panel: F_0/F_{CCCP} mean ± SD traces. Lower panel: Basal mtCEPIA2 signal intensity measured before CCCP treatment (right) and mitochondria Ca2+ efflux level after CCCP treatment calculated as F_0/F_{CCCP}. Data presented as box-and-whisker plots (box: 25th–75th percentile; whiskers: min to max), with each dot representing an individual larva (*n* = 13–14). Statistical analysis: *t*-test or Mann–Whitney test.

E) Decreased mitochondrial membrane potential in *tmbim5*$^{-/-}$ zebrafish observed in vivo in the optic tectum of 2 dpf larvae. Zebrafish embryos were injected with TMRE (1 nl of 2 mM) at the 1-cell stage and imaged in vivo using LSFM at 2 dpf. CCCP (10 µM) was used to depolarize mitochondria, and the F_0/F_{CCCP} ratio was calculated. Left: representative images of the ROI at

the beginning and after 5 min of CCCP treatment. Right: mitochondrial membrane potential (MMP), calculated as the F_0/F_{CCCP} ratio, is plotted as box-and-whisker plots (box: 25th–75th percentile; whiskers: min to max), with each dot representing an individual larva (*n* = 14–18). Statistical analysis: Mann–Whitney test.

Because of these difficulties, we decided to quantify Ca^{2+} content by exposing immobilized living zebrafish larvae to the uncoupling agent CCCP which induces mitochondrial depolarization and, as a consequence, a release of Ca^{2+} from mitochondria. No differences between *tmbim5*$^{+/+}$ and *tmbim5*$^{-/-}$ larvae were observed implying that Tmbim5 deficiency in larvae had no major effect on mitochondrial Ca^{2+} levels *in vivo* (Fig. 3C-D). Experiments boosting Ca^{2+} influx with glutamate added to the bath were not successful. These results imply that *in vivo* matrix Ca^{2+} levels under conditions of physiological cytosolic Ca^{2+} levels are not affected by Tmbim5. To corroborate this, we also measured Ca^{2+} efflux upon depolarization with CCCP *ex vivo* in isolated mitochondria, quantifying extramitochondrial Ca^{2+} levels using a specific dye. CCCP treatment results in release of all matrix Ca^{2+} and reflects mitochondrial Ca^{2+} levels. Consistent with our *in vivo* measurements using CEPIA2mt, this approach revealed no differences in Ca^{2+} levels between WT and *tmbim5*$^{-/-}$ mitochondria (Fig. EV3). To further investigate mitochondrial function in the brain of *tmbim5*$^{-/-}$ larvae, we injected tetramethylrhodamine ethyl ester (TMRE) into the yolk of zebrafish embryos at the 1-cell stage as described in (Vicente *et al*, 2019) to determine whether loss of Tmbim5 affects the mitochondrial membrane potential. TMRE is a positively charged dye known to accumulate in mitochondria due to their membrane potential. Two days after injection, we observed a TMRE signal similar to the CEPIA2mt pattern (Fig. 3C), which was significantly reduced after depolarisation with CCCP (Fig. 3E). We observed a smaller drop in TMRE signal intensity in *tmbim5*$^{-/-}$ larvae in response to depolarisation, indicating reduced dye accumulation within mitochondria and suggesting a reduced mitochondrial membrane potential in the brain of Tmbim5-deficient larvae (Fig. 3E). Together these findings suggest a potential mitochondrial dysfunction but no major differences in baseline mitochondrial Ca^{2+} concentration in Tmbim5-deficient fish.

Fish deficient in Mcu and Tmbim5 are viable and have no obvious phenotype

The MCU complex is the major mitochondrial Ca^{2+} uptake mechanism (Baughman *et al*, 2011; De Stefani *et al*, 2011). To clarify whether Tmbim5, as overexpression results suggested (Zhang *et al*, 2023), can act as an additional Ca^{2+} uptake mechanism besides the MCU complex or modify MCU activity, we crossed *tmbim5*$^{-/-}$ mutants with *mcu* KO fish hypothesizing that depletion of two (potentially independent) uptake mechanisms would be detrimental and/or alter mitochondrial Ca^{2+} uptake. Lack of changes in mitochondrial Ca^{2+} levels do not rule out changes in uptake capacity because these could be compensated by changes in efflux. *mcu* KO fish lack the capacity to uptake mitochondrial Ca^{2+} but have an otherwise unremarkable phenotype (Soman *et al*, 2019a). We here found no differences in mortality between *tmbim5*$^{+/+}$;*mcu*$^{-/-}$ and *tmbim5*$^{-/-}$;*mcu*$^{-/-}$ larvae (Fig. 4A) or in the distribution of adult zebrafish genotypes following a heterozygous cross (Fig. 4B) suggesting no additive detrimental effect. We also measured mitochondrial Ca^{2+} uptake in isolated mitochondria by quantifying external Ca^{2+} levels in the bath (Fig. 4C) and did not observe any effect of *tmbim5* knockout on Ca^{2+} uptake. These experiments, however, confirmed the previous observation that mitochondria from Mcu-deficient zebrafish show almost no Ca^{2+} uptake (Soman *et al*, 2019a). Together these results imply that Tmbim5 does not constitute a relevant mitochondrial Ca^{2+} uptake system independent of Mcu. It does not rule out a modulatory effect of Tmbim5 on the MCU complex.

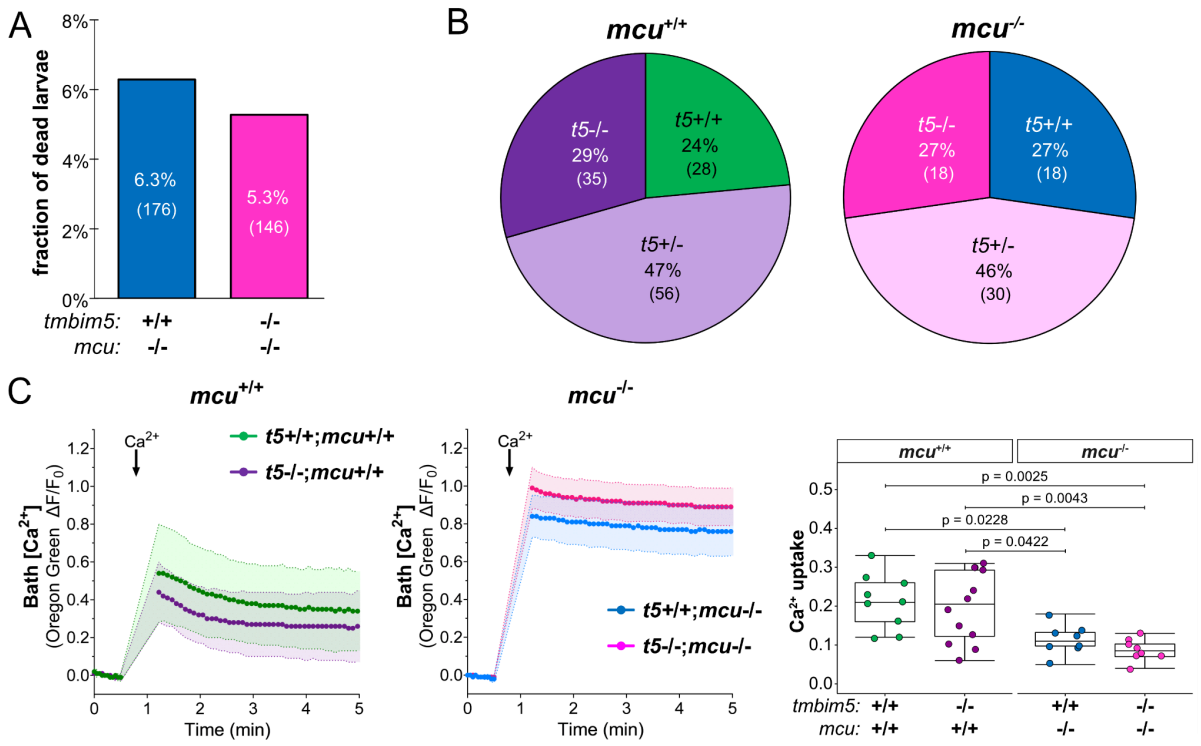

Figure 4. Fish deficient in Mcu and Tmbim5 are viable and have no obvious phenotype

A) Mortality of double knockout (*tmbim5*$^{-/-}$;*mcu*$^{-/-}$) larvae until 5 dpf does not differ from *tmbim5*$^{+/+}$;*mcu*$^{-/-}$. *n* is indicated in brackets. Number of experiments = 4. Statistical analysis: Chi-square test.

B) Genotype distribution does not deviate from the expected Mendelian ratio after *tmbim5*$^{+/-}$;*mcu*$^{+/-}$ zebrafish breeding. *n* is indicated in brackets. Statistical analysis: Chi-square test.

C) Loss of *Tmbim5* does not significantly affect mitochondrial Ca^{2+} uptake in mitochondria isolated from *mcu*$^{-/-}$ larvae. Mitochondria were loaded with Ca^{2+} (20 µM), revealing significantly reduced Ca^{2+} uptake in both single *mcu*$^{-/-}$ and double *tmbim5*$^{-/-}$;*mcu*$^{-/-}$ knockouts. Fluorescence of Oregon Green 488 BAPTA-5N was normalized to the initial value (F_0). Data are presented as mean ± SD $\Delta F/F_0$ traces. Gaps in the measurements are due to technical limitations of the equipment and procedure, which required pauses in fluorescence readings during reagent addition. On the right: quantification of Ca^{2+} uptake, calculated within 2 min after $CaCl_2$ addition as the difference between the maximum $\Delta F/F_0$ value after Ca^{2+} addition and the $\Delta F/F_0$ value reached 2 min later. Results are presented as box-and-whisker plots (box: 25th–75th percentile; whiskers: min to max), with each dot representing an independent biological replicate (*n* = 8–12). Statistical analysis: one-way ANOVA followed by post-hoc Tukey HSD test.

No changes in the mitochondrial Ca^{2+} uptake machinery in Tmbim5-deficient larvae

To investigate potential compensatory mechanisms active in Tmbim5-deficient larvae, we quantified the mRNA expression levels of proteins involved in mitochondrial Ca^{2+} handling, specifically Mcu, Micu1-3, Efhd1 (recently shown to interact with Mcu and suppress uniporter activity (Meng *et al*, 2023; Delgado de la Herran *et al*, 2024)), Letm1, and its paralogue Letm2, *slc8b1* (the probable NCLX ortholog) and Tmem65, which has been recently considered to be involved in Ca^{2+} efflux from mitochondria (Zhang *et al*, 2023; Vetralla *et al*, 2023; Garbincius *et al*, 2023). *Slc25a28*, which encodes Mitoferrin-2, a Ca^{2+}-independent transporter present in the mitochondrial inner membrane, served as control. We found no statistical relevant changes of any of these in *tmbim5*$^{-/-}$ larvae suggesting that the loss of Tmbim5 is not compensated by transcriptional upregulation of other components within the mitochondrial Ca^{2+} transport system. However, most transcripts appeared to be reduced in *tmbim5*-deficient larvae and analysis using two-way ANOVA indeed demonstrated a significant overall genotype effect on mitochondrial Ca^{2+} transport proteins in *tmbim5*$^{-/-}$ larvae (*p*=0.01681, Fig. EV4A). We therefore investigated the mitochondrial DNA (mtDNA) to

nuclear DNA (nDNA) ratio to assess potential alterations in mitochondrial content (Fig. EV4B-D). Quantitative analysis revealed no significant changes in mtDNA:nDNA ratio in whole *tmbim5*$^{-/-}$ larvae (Fig. EV4B) or adult zebrafish muscle tissue (Fig. EV4D). However, we detected a significant reduction in mitochondrial DNA content specifically in brain tissue of adult *tmbim5*$^{-/-}$ fish (Fig. EV4C). These findings suggest that Tmbim5 deficiency may impact mitochondrial mass or mitochondrial DNA replication in a tissue-specific manner, with more pronounced effects in neural tissues but not in muscle or whole-organism samples.

Knockout of *slc8b1* attenuates sodium-dependent mitochondrial Ca^{2+} release

Two recent publications suggested that TMBIM5 constitutes an additional mitochondrial Ca^{2+} efflux system (Patron *et al*, 2022; Austin *et al*, 2022) besides sodium-dependent mitochondrial Ca^{2+} release mediated by NCLX (Palty *et al*, 2010). Based on the hypothesis that concurrent disruption of dual mitochondrial Ca^{2+} efflux pathways would significantly compromise cellular function, we investigated the effects of NCLX inhibition in the context of Tmbim5 deficiency. Previous studies in cellular models demonstrated that TMBIM5 deletion combined with pharmacological inhibition of NCLX via CGP-37157 or *NCLX* knockdown by siRNA resulted in impaired mitochondrial Ca^{2+} buffering capacity (Austin *et al*, 2022; Patron *et al*, 2022). To study this in our zebrafish model, we first evaluated the efficacy of CGP-37157 on Na^{+}-dependent mitochondrial Ca^{2+} efflux, as this compound's activity had not been previously characterized in zebrafish. Contrary to expectations, CGP-37157 administration did not significantly alter Na^{+}-dependent Ca^{2+} efflux kinetics in mitochondria isolated from either wild-type or *tmbim5*$^{-/-}$ larvae (Fig. EV5). These findings indicate that under our experimental conditions, CGP-37157 lacks sufficient inhibitory activity against the zebrafish mitochondrial Na^{+}/Ca^{2+} exchanger, highlighting potential species-specific pharmacological differences.

We therefore generated a double-knockout zebrafish line lacking both Tmbim5 and the predicted Nclx to answer our question. The identity of NCLX in fish is unknown but the *slcb81* gene encodes a 308 amino acid protein with the highest homology (24%) to human NCLX and a predicted sodium/calcium exchanger domain at its N-terminus (Fig. EV6A). It is noteworthy that the predicted fish protein is only half as big as human NCLX which has a length of 584 amino acids. We designed a gRNA to target the conserved exchanger domain which led to the insertion of 17 bp resulting in a frameshift mutation, disrupting the proposed transporter function of Slc8b1 (Fig. EV6B). This resulted in a decrease in *slc8b1* mRNA levels. There were no compensatory changes of *tmbim5* mRNA (Fig. EV6C). s*lc8b1* (*nclx*) mRNA levels peaked at six hours post fertilization and declined thereafter in wildtype embryos (Fig. 5A). In situ hybridization revealed that *slc8b1* is strongly expressed in the brain and in neuromasts, which are sensory patches distributed on the head and along the lateral line of fish (Metcalfe *et al*, 1985) (Fig. 5B). In adult fish, *tmbim5* and *slc8b1* are both expressed in the brain but *slc8b1* is not expressed in skeletal muscles (Fig. 5C). These results suggest some but no complete overlap of the expression patterns of *tmbim5* and *slc8b1*. To assess whether Slc8b1 mediates Na^{+}-dependent Ca^{2+} efflux from mitochondria, we measured bath Ca^{2+} levels in mitochondria isolated from WT and *slc8b1*$^{-/-}$ larvae. After loading mitochondria with Ca^{2+}, MCU-mediated uptake was inhibited with Ru360, followed by stimulation of Na^{+}-dependent Ca^{2+} efflux with a Na^{+}-containing buffer (Fig. 5D). *slc8b1*$^{-/-}$ mitochondria had a similar Ca^{2+} uptake (Fig. 5E) and response to Ru360 (Fig. 5F). However, sodium-dependent Ca^{2+} efflux (Fig. 5G) was significantly impaired supporting Slc8b1 as a key component of this process and a likely NCLX ortholog. This suggests that Slc8b1 is a bona fide NCLX protein.

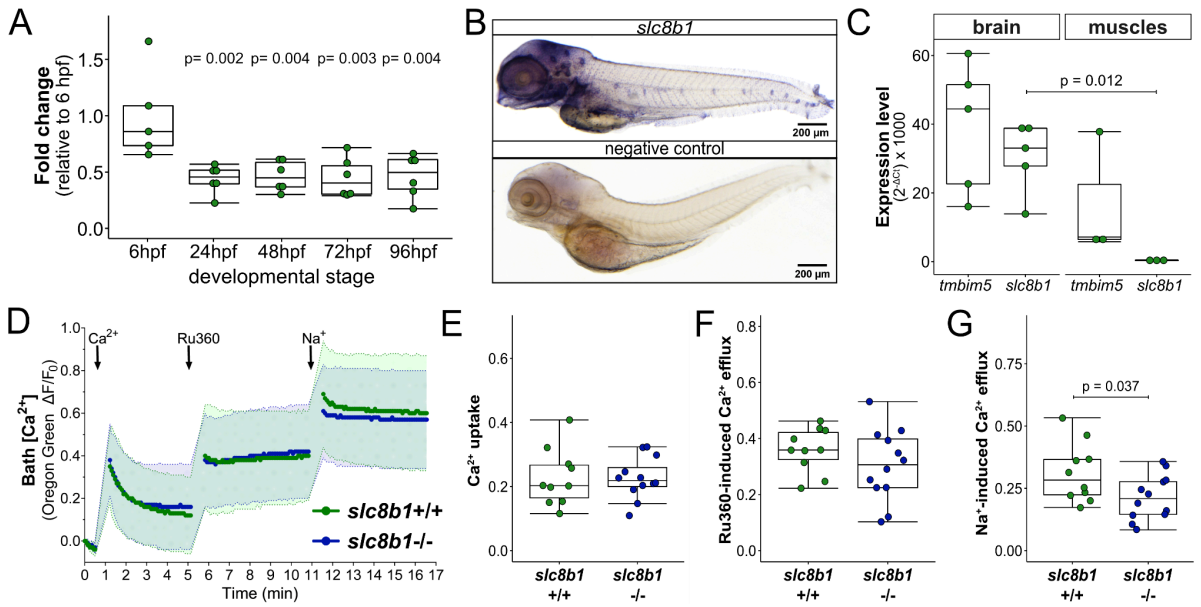

Figure 5. Impaired Na^+-dependent Ca^{2+} efflux in Slc8b1 lacking mitochondria.

A) *slc8b1* mRNA expression at different developmental stages, quantified using qPCR. Expression was normalized to 6 hours post-fertilization (hpf), with *18S* used as a reference gene. Results are shown as box-and-whisker plots (box: 25th–75th percentile, whiskers: min–max), with each dot representing an independent biological replicate (*n* = 5–6, each RNA sample pooled from 30 embryos). Statistical analysis: one-way ANOVA with post-hoc Tukey HSD test (*p*-values for comparisons with 6 hpf).

B) *slc8b1* transcript detected by whole-mount in situ hybridization (WISH) in 4 days post-fertilization (dpf) wild-type zebrafish. A sense probe was used as a negative control. Number of experiments = 3.

C) Comparative expression of *slc8b1* and *tmbim5* in the brain and skeletal muscles of adult zebrafish, assessed by qPCR. Data presented as box-and-whisker plots, each dot representing an independent biological replicate (*n* = 3–5, each RNA sample pooled from 2 fish). Statistical analysis: *t*-test with Benjamini-Hochberg (BH) correction for multiple comparisons.

D-G) Functional analysis of mitochondrial Ca^{2+} transport in mitochondria isolated from *slc8b1*$^{-/-}$ and WT larvae, using Oregon Green 488 BAPTA-5N fluorescence measurements.D) Changes in bath Ca^{2+} levels measured under basal conditions and after treatment with Ru360 (10 µM) to inhibit mitochondrial Ca^{2+} uptake. Upon addition of Na^+ (10 mM), a reduced Na^+-dependent Ca^{2+} efflux was observed in *slc8b1*$^{-/-}$ mitochondria. Fluorescence was normalized to initial values (F_0), and data are presented as mean ± SD $\Delta F/F_0$ traces. E) *slc8b1* knockout does not affect Ca^{2+} uptake into mitochondria. Quantification of mitochondrial Ca^{2+} uptake was performed 2 min after $CaCl_2$ addition. F) No significant difference in Ca^{2+} efflux following Ru360 treatment. Efflux was estimated by subtracting the last $\Delta F/F_0$ value after $CaCl_2$ addition from the maximum $\Delta F/F_0$ after Ru360 addition. G) Reduced Ca^{2+} efflux from *slc8b1-/-* mitochondria after Na^+ addition compared to WT. Efflux was quantified as the difference between the last $\Delta F/F_0$ value after Ru360 addition and the maximum $\Delta F/F_0$ after Na^+ addition.

Results (D-G) are presented as box-and-whisker plots, with each dot representing an independent biological replicate (*n* = 10–12). Statistical analysis: *t*-test.

Mild organismal phenotype in tmbim5/slc8b1 double knockout fish despite severe impairment of mitochondrial Ca^{2+} handling and ultrastructural abnormalities

Having established Slc8b1 as a relevant mitochondrial Ca^{2+} efflux system, we next clarified whether removal of both transport systems is deleterious. The Mendelian distribution of offspring was as expected (Fig. 6A) but we noticed an increased mortality of *slc8b1*$^{-/-}$ fish at the larval stage which was surprisingly rescued by *tmbim5*$^{-/-}$;*slc8b1*$^{-/-}$ double KO (Fig. 6B). Larval body length, eye diameter and somite thickness (Fig. 6C), spontaneous (Fig. 6D) and light-induced locomotor activity (Fig. 6E) of wildtype, *slc8b1*$^{-/-}$ and *tmbim5*$^{-/-}$;*slc8b1*$^{-/-}$ larvae were all similar.

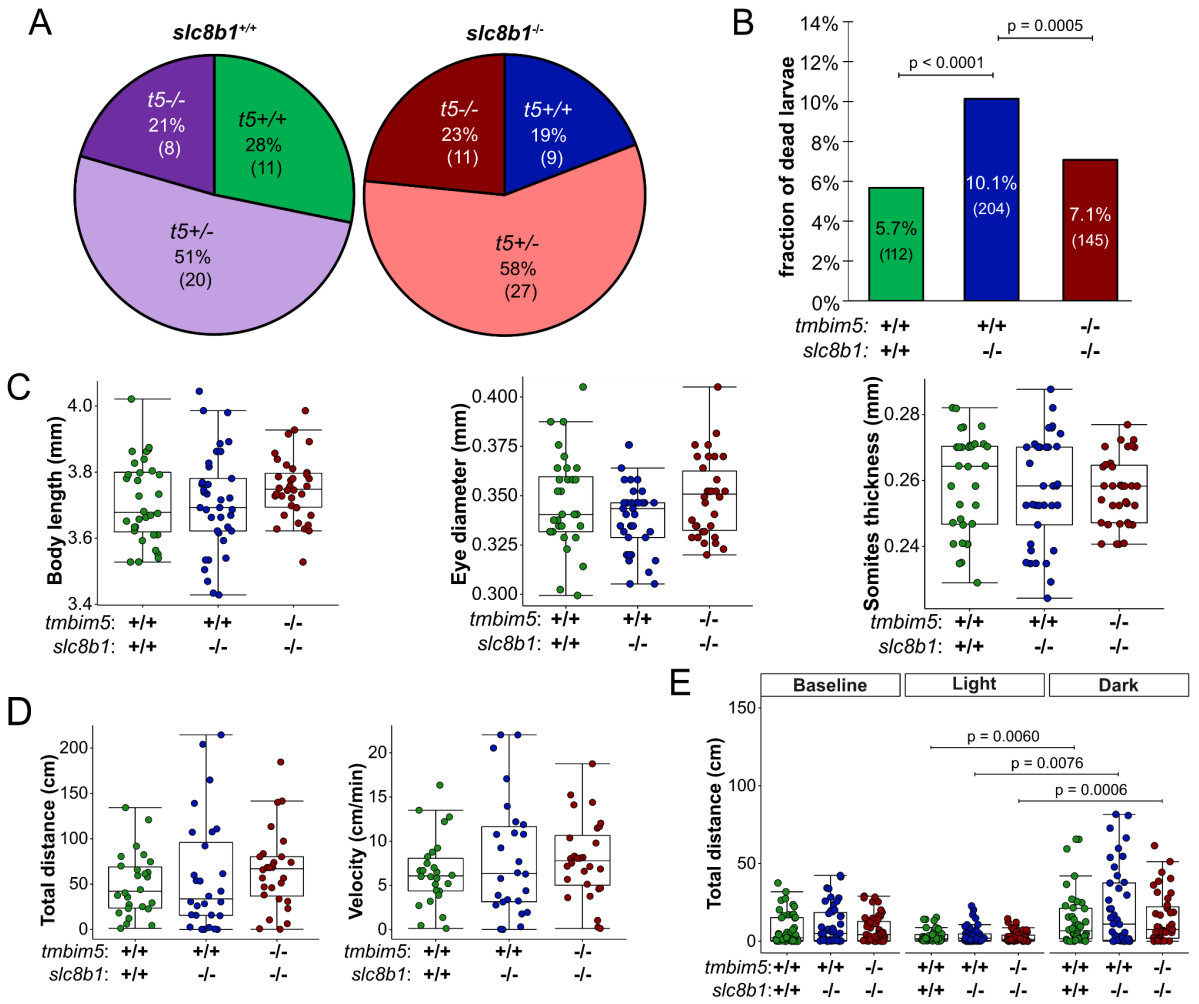

Figure 6. Mild organismal phenotype in tmbim5/slc8b1 double knockout fish despite severe impairment of mitochondrial Ca2+ handling and ultrastructural abnormalities

A) Genotype distribution of offspring from *tmbim5*$^{+/-}$;*slc8b1*$^{+/-}$ zebrafish breeding does not differ from expected Mendelian ratios. Sample sizes are indicated in brackets. Statistical analysis: Chi-square test, number of experiments = 3.

B) Mortality of *slc8b1*$^{-/-}$ larvae until 5 dpf is lower compared to wild-type or *tmbim5*$^{-/-}$;*slc8b1*$^{-/-}$ double KO larvae. Sample sizes are indicated in brackets. Statistical analysis: Chi-square test.

C) Normal morphology and body size of *slc8b1*$^{-/-}$ and *tmbim5*$^{-/-}$;*slc8b1*$^{-/-}$ larvae at 5 dpf. Morphometric measurements (body length, eye diameter, and somite thickness) are presented as box-and-whisker plots (box: 25th–75th percentile, whiskers: min–max), with each dot representing an individual larva (*n* = 32–34). Statistical analysis: one-way ANOVA with post-hoc Tukey HSD test (body length and eye diameter) or Kruskal-Wallis test with Dunn's post-hoc test (somite thickness). Number of experiments = 3.

D) Locomotor activity of 5 dpf larvae in an open-field test is not affected by *slc8b1* KO or *tmbim5*$^{-/-}$;*slc8b1*$^{-/-}$ double KO. Total distance traveled and mean velocity are plotted as box-and-whisker plots (box: 25th–75th percentile, whiskers: min–max), with each dot representing an individual larva (*n* = 26–28). Statistical analysis: Kruskal-Wallis test followed by Dunn's post-hoc test. Number of experiments = 2.

E) Normal visual-motor response of *slc8b1*$^{-/-}$ and *tmbim5*$^{-/-}$;*slc8b1*$^{-/-}$ larvae at 5 dpf. Total distance traveled during each phase of the experiment is presented as box-and-whisker plots (box: 25th–75th percentile, whiskers: min–max), with each dot representing an individual larva (*n* = 40–48). Statistical analysis: two-way ANOVA followed by Kruskal-Wallis test and Dunn's post-hoc test. Number of experiments = 2.

To further elucidate the functional interplay between Tmbim5 and Slc8b1, we conducted a comprehensive analyses of mitochondrial Ca^{2+} transport dynamics and ultrastructural morphology. Quantitative assessment of Ca^{2+} flux revealed significant perturbations in *tmbim5*/*slc8b1* double knockout mitochondria, characterized by attenuated Ca^{2+} uptake capacity and diminished responsiveness to both Ru360 inhibition and Na^{+}-stimulated efflux

(Fig. 7A). These functional abnormalities corresponded with pronounced alterations in mitochondrial ultrastructure that were only present in the double knockout animals (Fig. 7E). These findings align with previous data from HEK cells demonstrating that combined TMBIM5 and NCLX dysfunction leads to compromised mitochondrial Ca^{2+} handling capacity (Patron *et al*, 2022; Austin *et al*, 2022) and impaired ruthenium red-sensitive Ca^{2+} efflux (Austin *et al*, 2022). Our results are therefore in line with the assumption that TMBIM5 facilitates mitochondrial Ca^{2+} influx, particularly when NCLX-mediated efflux is compromised. This suggests that the dysregulated mitochondrial Ca^{2+} homeostasis resulting from simultaneous disruption of these pathways may directly contribute to the observed ultrastructural abnormalities. The disconnect between severe subcellular abnormalities and mild organismal phenotypes underscores the remarkable adaptability of mitochondrial Ca^{2+} homeostatic systems *in vivo*.

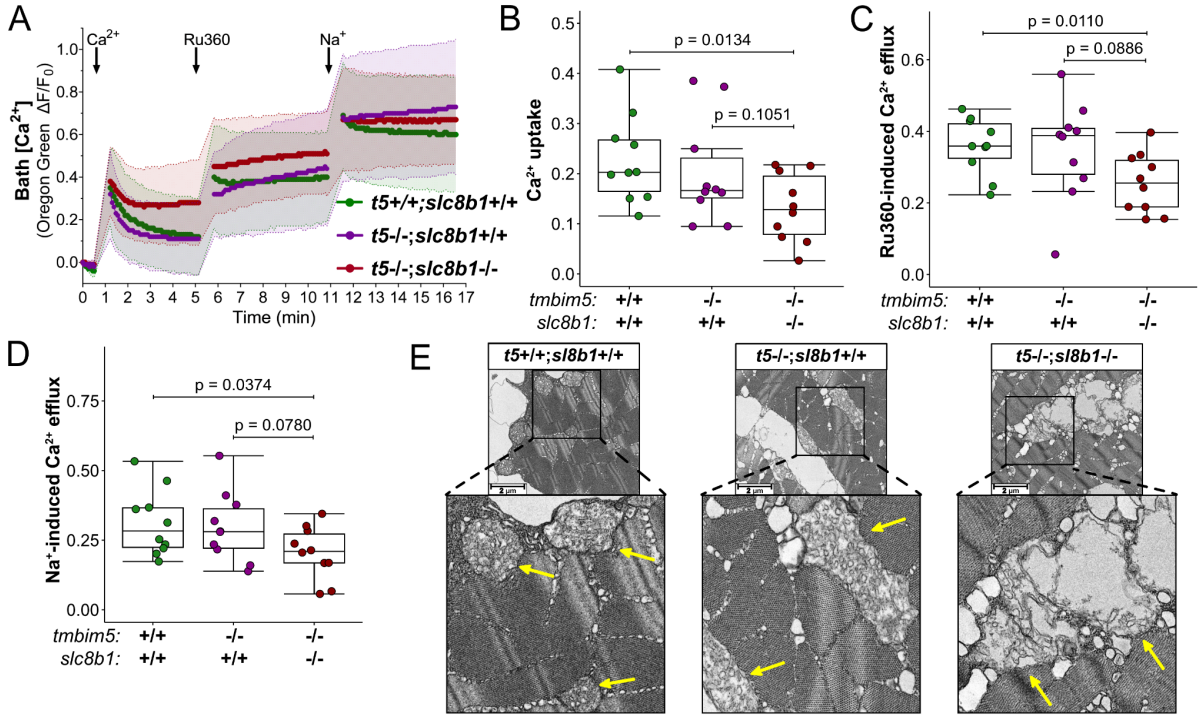

Figure 7. Impaired mitochondrial Ca^{2+} uptake and aberrant mitochondrial morphology in *tmbim5*$^{-/-}$;*slc8b1*$^{-/-}$ double knockout larvae.

A) Changes in bath Ca^{2+} measured by Oregon Green 488 BAPTA-5N in mitochondria isolated from wild-type (WT), *tmbim5*$^{-/-}$, and *tmbim5*$^{-/-}$*;slc8b1*$^{-/-}$ larvae. Mitochondria were first loaded with Ca^{2+} (20 μM), followed by the addition of Ru360 (10 μM) to inhibit Ca^{2+} influx. Next, Na^+ (10 mM) was added to assess Ca^{2+} efflux via NCLX activity, showing reduced Na^+-dependent Ca^{2+} efflux in *slc8b1*$^{-/-}$ mitochondria. Fluorescence was normalized to the initial value (F_0). Data are presented as mean ± SD $\Delta F/F_0$ traces.

B) Reduced Ca^{2+} uptake by mitochondria from *tmbim5*$^{-/-}$*;slc8b1*$^{-/-}$ larvae compared to WT. Ca^{2+} uptake was quantified 2 minutes after $CaCl_2$ addition.

C) Decreased Ca^{2+} efflux from mitochondria isolated from *tmbim5*$^{-/-}$*;slc8b1*$^{-/-}$ larvae. The amount of Ca^{2+} efflux after Ru360 addition was estimated by subtracting the last $\Delta F/F_0$ value obtained after $CaCl_2$ addition from the maximal $\Delta F/F_0$ value after Ru360 addition.

D) Reduced Na^+-dependent Ca^{2+} efflux in mitochondria from *tmbim5*$^{-/-}$*;slc8b1*$^{-/-}$ larvae compared to WT. The amount of Ca^{2+} efflux following Na^+ addition was estimated by subtracting the last $\Delta F/F_0$ value obtained after Ru360 addition from the maximal $\Delta F/F_0$ value after Na^+ addition.

B-D) Results are presented as box-and-whisker plots (box: 25th–75th percentile, whiskers: min–max), with each dot representing an independent biological replicate (n = 10). Statistical analysis: two-way ANOVA followed by *t*-test or Mann–Whitney test.

E) Aberrant mitochondrial morphology in *tmbim5*$^{-/-}$*;slc8b1*$^{-/-}$ double knockout larvae. Representative transmission electron microscopy images of mitochondria from skeletal muscles of 5 dpf WT, *tmbim5*$^{-/-}$, and *tmbim5*$^{-/-}$*;slc8b1*$^{-/-}$ zebrafish larvae. Arrows indicate mitochondria in magnified images.

Discussion

Our findings establish Tmbim5 as critical for growth, muscle function, and mitochondrial membrane potential maintenance in zebrafish, despite not affecting steady-state mitochondrial Ca^{2+} levels. Combined deletion of *tmbim5* and *mcu* produced no significant phenotypic or functional consequences, whereas concurrent ablation of *tmbim5* and the putative NCLX ortholog *slc8b1* resulted in altered mitochondrial Ca^{2+} handling dynamics and ultrastructural abnormalities without manifesting a severe organismal phenotype. These results suggest that Tmbim5 probably predominantly functions in mitochondrial Ca^{2+} efflux pathways and indicate the existence of additional, yet uncharacterized mitochondrial Ca^{2+} transport mechanisms.

Tmbim5 deficiency decreased the size of zebrafish larvae and weight of adults in line with knockdown of the *tmbim5* ortholog in snails (Yu *et al*, 2020) but not in mice (Zhang *et al*, 2022). However, similar to *Tmbim5* mutant mice that suffer from myopathy, myofiber cross-sections were smaller in *tmbim5*$^{-/-}$ fish, indicating muscle atrophy. This was particularly pronounced in slow-twitch muscles, which contain abundant mitochondria and rely heavily on oxidative phosphorylation compared to fast-twitch fibers (Control of muscle fibre-type diversity during embryonic development: The zebrafish paradigm, 2013), suggesting a direct link with compromised mitochondrial function. These pathological alterations of muscle function probably underlie the delayed escape of Tmbim5-deficient embryos from the chorion which is mediated by tail coiling (Lessman & Carver, 2014). Interestingly, *Mcu* knockout in mice also negatively affects size (Pan *et al*, 2013) and affects proper skeletal muscle trophism (Mammucari *et al*, 2015; Gherardi *et al*, 2019). MICU1-deficient mice also showed severe growth defects (Liu *et al*, 2016) and marked muscle weakness, easy fatigue and smaller muscle fibers (Liu *et al*, 2016; Debattisti *et al*, 2019). In addition, loss-of-function mutations in human *MICU1* are associated with myopathy (Logan *et al*, 2014; Lewis-Smith *et al*, 2016; Bitarafan *et al*, 2021). Together these observations corroborate the role of Tmbim5 in the regulation of growth and muscle function and point out similarities between the effects of Tmbim5, Mcu and Micu1 loss.

Two recent studies demonstrated that TMBIM5 functions as a pH-dependent mitochondrial Ca^{2+} efflux transporter (Patron *et al*, 2022; Austin *et al*, 2022). Zhang et al., in contrast, found that TMBIM5 overexpression in HEK cells enhanced mitochondrial Ca^{2+} uptake following ER Ca^{2+} release (Zhang *et al*, 2022), suggesting that TMBIM5 may operate bidirectionally under certain conditions. To clarify the physiological relevance of this, we now generated two

double knockout zebrafish lines: one lacking both Tmbim5 and Mcu, the primary mitochondrial Ca^{2+} influx mediator, and another deficient in Tmbim5 and Slc8b1, the zebrafish ortholog of NCLX, the major mitochondrial Ca^{2+} efflux pathway. Surprisingly, both double knockout lines were viable and exhibited no overt organismal phenotypic alterations.

The absence of enhanced mitochondrial Ca^{2+} uptake deficits in *tmbim5*/*mcu* double knockout zebrafish argues against Tmbim5 functioning as a primary Ca^{2+} influx channel capable of compensating loss of Mcu function, as this would have likely caused a more severe phenotype and would have reduced Ca^{2+} uptake independently of Mcu function. Two alternative mechanisms remain plausible to reconcile these data with previous reports: First, Tmbim5 may facilitate Ca^{2+} transport specifically at high Ca^{2+} concentrations. The increased uptake observed in TMBIM5-overexpressing cells after ATP stimulation (Zhang et al., 2022) might be relevant at mitochondria-ER contact sites where local Ca^{2+} reaches up to 100 μM – conditions not tested in our system. Second, Tmbim5 may function as a regulatory modifier of MCU complex activity rather than as an autonomous Ca^{2+} influx channel. This hypothesis is supported by recent proteomic analyses identifying Tmbim5 as a component of the MCU interactome (Delgado de la Herran *et al*, 2024). The normal mitochondrial Ca^{2+} uptake observed in Tmbim5-deficient mitochondria also argues against significant alteration of MCU complex function through the proposed AFG3L2-EMRE regulatory axis. While Tmbim5 inhibits the m-AAA protease AFG3L2 (Patron *et al*, 2022), which mediates EMRE degradation (König *et al*, 2016; Tsai *et al*, 2017), our data suggest this pathway does not significantly impact MCU-mediated Ca^{2+} transport under our experimental conditions, despite its theoretical potential to reduce MCU complex stability through enhanced EMRE turnover.

The observed mitochondrial alterations in *tmbim5/slc8b1* double knockout zebrafish – impaired Ca^{2+} handling combined with disrupted cristae architecture – suggest that Tmbim5 plays a critical role in mitochondrial Ca^{2+} efflux pathways. The reduced Ca^{2+} uptake likely stems from compromised mitochondrial membrane potential, which provides the electrochemical driving force for Ca^{2+} accumulation in the mitochondrial matrix. This also aligns with the observed ultrastructural abnormalities in these mitochondria but was not studied in our contribution. Our finding that Tmbim5 deficiency alone does not significantly alter cristae morphology contrasts with several published reports (Oka *et al*, 2008; Seitaj *et al*, 2020; Austin *et al*, 2022; Zhang *et al*, 2022) but corresponds with observations in HEK cells (Patron *et al*, 2022), suggesting potential cell type or species-specific differences in Tmbim5 function. The paradoxical absence of severe phenotypes in double knockout fish and the unexpected protective effect on larval mortality indicate robust compensatory mechanisms that maintain mitochondrial function despite disrupted Ca^{2+} homeostasis. These adaptive responses appear to operate in a developmentally regulated manner, potentially involving differential engagement of alternative Ca^{2+} transport systems, metabolic rewiring, or activation of stress response pathways at specific developmental stages.

Our study provides the first comprehensive characterization of zebrafish *slc8b1*, establishing its expression pattern, functional properties, and loss-of-function phenotype as the probable NCLX ortholog in this model organism. Similar to murine NCLX (Luongo *et al*, 2017), zebrafish *slc8b1* demonstrates predominant expression in neural tissues. Functional analyses confirm that Slc8b1 operates as a *bona fide* NCLX, as its depletion significantly attenuated Na^{+}-dependent mitochondrial Ca^{2+} efflux. Notably, residual Na^{+}-dependent efflux persists in *slc8b1*-deficient mitochondria, suggesting potential compensatory mechanisms or alternative transport pathways. The structural divergence between zebrafish Slc8b1 and its mammalian counterparts – with fish Slc8b1 being approximately half the size of human NCLX – also raises intriguing mechanistic questions. We propose that zebrafish Slc8b1 may

function as a homodimer or potentially interact with additional protein partners to constitute a fully functional NCLX complex. Remarkably, *slc8b1*-deficient zebrafish remain viable, contrasting with the embryonic lethality observed in Nclx-knockout mice (Luongo *et al*, 2017). This differential phenotypic impact parallels observations with MCU deficiency, which causes minimal phenotypic consequences in zebrafish (Soman *et al*, 2019b; Tomar *et al*, 2019; Langenbacher *et al*, 2020) but results in lethality in mice on the C57Bl/6 background (Murphy *et al*, 2014) These species-specific differences highlight important evolutionary divergence in mitochondrial Ca^{2+} homeostasis mechanisms and underscore the value of comparative model organism studies.

We conclude that this lack of a strong phenotype in double knockout fish for influx and efflux pathways suggests the presence of robust compensatory mechanisms or the existence of alternative pathways that can maintain mitochondrial Ca^{2+} homeostasis in the absence of Tmbim5 and Mcu/Slc8b1. So which other proteins could do the job? LETM1 has been postulated to mediate mitochondrial H^+-dependent Ca^{2+} efflux (Jiang *et al*, 2009) and LETM1-containing liposomes were able to accumulate Ca^{2+} (Jiang *et al*, 2009; Tsai *et al*, 2014; Shao *et al*, 2016), but its function as a Ca^{2+} transporter is still in dispute. Austin et al. observed that inhibiting the potassium-hydrogen exchanger with quinine reduced mitochondrial Ca^{2+} efflux. They interpreted this finding as evidence that LETM1 might influence mitochondrial Ca^{2+} efflux by directly regulating monovalent cation levels rather than by directly transporting Ca^{2+} itself (Austin *et al*, 2017). Interestingly, LETM1 might interact with TMBIM5 (Austin *et al*, 2022). Another recently identified candidate for Ca^{2+} efflux is TMEM65 (Garbincius *et al*, 2023; Vetralla *et al*, 2023; Zhang *et al*, 2023). However, TMEM65-mediated Ca^{2+} efflux can also be inhibited by CGP as well as by *NCLX* knockout, indicating that this protein is an essential NCLX regulator and not an independent transporter (Garbincius *et al*, 2023; Vetralla *et al*, 2023).

In conclusion, loss of Tmbim5 impairs zebrafish growth, increases cell death in the brain and results in abnormal mitochondrial function as evidenced by reduced mitochondrial membrane potential. However, the absence of Tmbim5 did not exacerbate the phenotype of either *mcu* or *slc8b1* knockout zebrafish despite functional and morphological changes in *tmbim5/slc8b1* double knockout fish. Thus, alternative pathway(s) of mitochondrial Ca^{2+} influx and efflux compensate for the loss of these proteins.

Methods

Reagents and Tools table

Reagent/Resource	**Reference or Source**	**Identifier or Catalog Number**
Experimental Models: *Danio rerio*		
AB (wild-type)	Zebrafish Core Facility, IIMCB, Poland	ZDB-GENO-960809-7
tmbim5 (*ghitm*)$^{-/-}$	(Gasanov *et al*, 2021) Prof. Jacek Kuźnicki, IIMCB, Poland	-
Tg(HuC:CEPIA2mt)	Prof. Jacek Kuźnicki, IIMCB, Poland	-
mcu$^{-/-}$	(Soman *et al*, 2019a)	-

Reagent/Resource	Reference or Source	Identifier or Catalog Number
	Prof. Jacek Kuźnicki, IIMCB, Poland	
slc8b1(nclx)$^{-/-}$	This study	-
Antibodies:		
Alkaline phosphatase-conjugated anti-DIG antibody	Roche	11093274910
Oligonucleotides and other sequence-based reagents:		
Oligonucleotides for gRNA synthesis gRNA for generation of *tmbim5*$^{-/-}$ line	(Gasanov *et al*, 2021)	-
Primers for *tmbim5*$^{-/-}$ genotyping	(Gasanov *et al*, 2021)	-
Oligonucleotide for gRNA synthesis for generation of *slc8b1*$^{-/-}$ line	This study Sigma-Aldrich	TAATACGACTCACTATAGGAGTGACGTTC CTGGCTCTGTTTTAGAGCTAGAA
Constant oligonucleotide for gRNA synthesis	(Gasanov *et al*, 2021)	-
Primers for *slc8b1*$^{-/-}$ genotyping by HRM: FW	This study Sigma-Aldrich	GTGTACCATGTGGATGTGTGTTG
Primers for *slc8b1*$^{-/-}$ genotyping by HRM: RV	This study Sigma-Aldrich	CAGACCAGCAGTTTGAGGGTG
Primers for *slc8b1*$^{-/-}$ genotyping by sequencing: FW	This study Sigma-Aldrich	GAGTTTGCCGTTTAATTTCTGG
Primers for *slc8b1*$^{-/-}$ genotyping by sequencing: RV	This study Sigma-Aldrich	AATTCCTCACCAAAAAGTGCTC
qPCR primers	This study	Table 1
Primers for riboprobe against *tmbim5* synthesis: FW	This study Sigma-Aldrich	CGCTGCTCAGAGGTGAAGGT
Primers for riboprobe against *tmbim5* synthesis: RV	This study Sigma-Aldrich	TAATACGACTCACTATAGGGATGTGTGCG GCATCTCTGCG
Primers for riboprobe against *slc8b1* synthesis: FW	This study Sigma-Aldrich	GTGTAGACGTGCGTTCTTGC
Primers for riboprobe against *slc8b1* synthesis: RV	This study Sigma-Aldrich	TAATACGACTCACTATAGGGACGAGACG CCACAGTAAA
Chemicals, Enzymes and other reagents		
N-phenylthiourea (PTU)	Alfa Aesar	103-85-5
Cas9	(Gasanov *et al*, 2021) Prof. Jacek Kuźnicki, IIMCB, Poland	-
Precision Melt Supermix	BioRad	1725112

Reagent/Resource	Reference or Source	Identifier or Catalog Number
MegaScript T7 Transcription Kit	Invitrogen™	A57622
Phenol red solution	Sigma-Aldrich	P0290
BioMix Red	BioLine	BIO-25006
TRI Reagent	Invitrogen™	AM9738
iScript™ cDNA Synthesis Kit	BioRad	1708891
SsoAdvanced Universal SYBR Green Supermix	BioRad	1725274
Phenylmethylsulfonyl fluoride (PMSF)	Roche	10837091001
Protein Assay Dye	Bio-Rad	5000006
Digoxigenin (DIG)-labeled UTP	Roche	11277073910
Paraformaldehyde	Sigma-Aldrich	P6148
Blocking Reagent	Roche	11096176001
Nitro-blue tetrazolium chloride (NBT)	Roche	11383213001
5-bromo-4-chloro-3-indolyl-phosphate (BCIP)	Roche	11383221001
Glycogen Assay Kit II (Colorimetric)	Abcam	ab169558
Acridine Orange (AO)	Sigma-Aldrich	A8097
Tricaine	Sigma	A-5040
Low-melting-point agarose	Sigma-Aldrich	A9414
CGP-37157	Sigma-Aldrich	220005
Carbonyl cyanide 3-chlorophenylhydrazone (CCCP)	Sigma-Aldrich	C2759
Ru360	Sigma-Aldrich	557440
Thapsigargin	Invitrogen™	T7459
Oregon Green™ 488 BAPTA-5N hexapotassium salt	Invitrogen™	O6812
Tetramethylrhodamine, Ethyl Ester, Perchlorate (TMRE)	Invitrogen™	T669
Dimethyl Sulfoxide (DMSO)	Sigma-Aldrich	D8418
Software		
Precision Melt Analysis™ Software	Bio-Rad	
SnapGene software	SnapGene	www.snapgene.com

Reagent/Resource	Reference or Source	Identifier or Catalog Number
CHOPCHOP	(Labun *et al*, 2019)	https://chopchop.cbu.uib.no
CRISPRscan	(Moreno-Mateos *et al*, 2015)	https://www.crisprscan.org
CFX Maestro Software	Bio-Rad	
ImageJ	(Schneider *et al*, 2012)	https://imagej.nih.gov/ij/
ZEN Microscopy software	Zeiss	
EthoVision XT software	Noldus	
R version 4.1.2		https://www.r-project.org
GraphPad Prism v8		https://www.graphpad.com
Other		
CFX Connect RT-PCR Detection System	BioRad	
Borosilicate glass capillaries	Sutter	B100-75-10
P-1000 Flaming/Brown micropipette puller	Sutter	
FemtoJet microinjector	Eppendorf	
ChemiDoc	BioRad	
Nikon SMZ25 stereomicroscope	Nikon	
Zeiss Lightsheet Z.1 microscope	Zeiss	
96-well half-area black polystyrene microplate	Corning®	CLS3694
Tecan Infinite M1000 Pro	Tecan	
Tecan Sunrise		
ZebraBox	ViewPoint	
ZebraCube	ViewPoint	

Methods and Protocols:

Animal Maintenance

tmbim5$^{+/+}$, *tmbim5*$^{-/-}$, *tmbim5*$^{+/+}$;Tg(*HuC:CEPIA2mt*), *tmbim5*$^{-/-}$;Tg(*HuC:CEPIA2mt*); *tmbim5*$^{+/+}$;*mcu*$^{-/-}$, *tmbim5*$^{-/-}$;*mcu*$^{-/-}$, *tmbim5*$^{+/+}$;*slc8b1*$^{-/-}$ and *tmbim5*$^{-/-}$;*slc8b1*$^{-/-}$ zebrafish were used in the study. All animals were maintained following previously described methods (Matthews *et al*, 2002) in the Zebrafish Core Facility, a licensed breeding and research facility (PL14656251, registry of the District Veterinary Inspectorate in Warsaw; 064 and 051, registry of the Ministry of Science and Higher Education) at the International Institute of Molecular and Cell Biology in Warsaw. Adult zebrafish and larvae were kept in E3 medium (2.48 mM NaCl, 0.09 mM KCl, 0.164 mM $CaCl_2 \cdot 2H_2O$, and 0.428 mM $MgCl_2 \cdot 6H_2O$) at 28.5

°C. Larvae were kept in a Petri dish (~50 larvae/dish) in an incubator under a 14 h/10 h light/dark cycle. The stages of fish development were defined as hours postfertilization (hpf) and days postfertilization (dpf). Zebrafish embryos, that were planned to be used in stainings or *in vivo* imaging experiments, were treated with N-phenylthiourea (PTU, Alfa Aesar Cat# 103-85-5) at final concentration of 0.003% to avoid pigmentation.

This study follows ARRIVE guidelines (Kilkenny *et al*, 2010). All experimental procedures were approved by the Local Ethical Committee for Experiments on Animals in Warsaw (permission no. WAW2/050/2022) and performed in accordance with European and Polish regulations on animal welfare.

Generation and genotyping of mutant and transgenic zebrafish lines

The generation of *tmbim5*$^{-/-}$ zebrafish using CRISPR-Cas9 gene editing was previously described in (Gasanov *et al*, 2021). Briefly, a mix of two gRNA: 5'-GGCTGGTATGTGGGAGTCTA-3' and 5'-CGCGGGCAGTGTGGGCCTGA-3' (0.04 mg/ml of each) and Cas9 protein (0.2 mg/ml) were injected into the cytoplasm of one-cell stage wild-type AB zebrafish embryos.

Fish were grown up after injections up to 4-months-old and were fin-clipped for DNA sampling and high resolution melting (HRM) analysis. Targeted region in the 4th exon of *tmbim5* was amplified using Precision Melt Supermix (BioRad, Cat# 1725112), primers: *tmbim5 HRM forward*: 5'-CGATCTGGCCGCAGTACG-3', *tmbim5 HRM reverse*: 5'-CCAGCCAGGAGTTGCTC-3' and the CFX Connect RT-PCR Detection System (BioRad). Melting curve analysis was performed using Precision Melt Analysis (Bio-Rad) software. The mutation-positive ones were analyzed by DNA sequencing. Fish with the deletion of 29 nucleotides and premature STOP codon was selected as F0 founder. F0 fish was outcrossed with the AB zebrafish line, and their mutation-carrying offspring were in-crossed to generate homozygous mutants. Fish were screened via PCR using the same primers as for HRM analysis, followed by Sanger sequencing.

Genotyping of subsequent generations of *tmbim5*$^{+/+}$, *tmbim5*$^{+/-}$ and *tmbim5*$^{-/-}$ fish was based on the difference in the size of PCR product that was detected by electrophoresis in 2% agarose.

To generate double knockout of *tmbim5* and *mcu*, tmbim5-/- zebrafish were outcrossed with *mcu*$^{-/-}$ zebrafish (obtained as a kind gift from prof. Jacek Kuźnicki laboratory). Obtained heterozygous fish were incrossed and their offspring was genotyped for *tmbim5* as described above and for *mcu* as described in (Soman *et al*, 2019a).

To generate zebrafish knockout of *nclx* the exon 5 of *slc8b1* gene was targeted with gRNA designed with free web tools: CHOPCHOP (Labun *et al*, 2019) and CRISPRscan (Moreno-Mateos *et al*, 2015) according to the protocol described in (Wiweger *et al*, 2021). Sequences that were common in both of the predictions and were scored as low risk for off-targets were chosen. The correctness of the sequence in the targeted area in the AB zebrafish was confirmed by Sanger sequencing. The gene-specific oligonucleotide with T7 overlaps: 5'-taatacgactcactataGGAGTGACGTTCCTGGCTCTgttttagagctagaa-3'. During gRNA preparation, annealing and filling in steps were combined, and the template was prepared by PCR using BioMix Red (BioLine, Cat# BIO-25006), gene-specific and constant oligo: 5'-AAAAGCACCGACTCGGTGCCACTTTTTCAAGTTGATAACGGACTAGCCTTATTTTAACTTGCTATTTCTAGCTCTAAAAC-3' (10 µM). The PCR conditions were the following: pre-incubation at 95°C for 3 min, followed by 35 cycles of 95°C for 15 s, 40°C for 15 s, and 68°C for 15 s. sgRNA was prepared using 150 ng of purified PCR product and MegaScript T7 Transcription Kit (Invitrogen, Cat# A57622) according to the manufacturer's

recommendations. Thereafter, RNA was precipitated by overnight incubation with ammonium acetate at -20°C.

gRNA was suspended in water, and the concentration was adjusted to 500 ng/µl. Cas9 protein (14 mg/ml stock, made in-house) was diluted in KCl/HEPES (200 mM/10 mM, pH 7.5) buffer to a final concentration of 600 ng/µl. The injection mixture was assembled fresh by mixing 2 µl of gRNA (1 µg), 2 µl of Cas9 (1.2 µg), and 0.5 µl phenol red (Sigma, Cat# P0290) and left for complex formation at room temperature for 5–10 min. Thereafter, the samples were kept on ice. Microneedles were pulled from borosilicate glass capillaries (Sutter; Cat# B100-75-10) using a P-1000 Flaming/Brown micropipette puller (Sutter). One nanoliter of the gRNA/Cas9/phenol red mixture was injected into the yolk at 1–2 cell-stage *tmbim5*$^{-/-}$ zebrafish embryos using a FemtoJet microinjector (Eppendorf).

Fish were grown up after injections up to 4-months-old and were fin-clipped for DNA sampling and high resolution melting (HRM) analysis. Targeted region in the 5th exon of *scl8b1* was amplified using Precision Melt Supermix (BioRad, Cat# 1725112), primers: *slc8b1 HRM forward*: 5'-GTGTACCATGTGGATGTGTGTTG-3', *slc8b1 HRM reverse*: 5'-CAGACCAGCAGTTTGAGGGTG-3' and the CFX Connect RT-PCR Detection System (BioRad). Melting curve analysis was performed using Precision Melt Analysis (Bio-Rad) software. The mutation-positive ones were analyzed by DNA sequencing of PCR products. Samples for sequencing were prepared by PCR using BioMix Red (BioLine, Cat# BIO-25006), *slc8b1 seq forward*: 5'-GAGTTTGCCGTTTAATTTCTGG-3', *slc8b1 seq reverse*: 5'-AATTCCTCACCAAAAAGTGCTC-3' and 2 µl of gDNA template per 20 µl of reaction. Fish with the confirmed insertions or deletions leading to premature STOP codon were selected as F0 founders. F0 fish was outcrossed with the AB zebrafish line, and their mutation-carrying offspring were in-crossed to generate double-homozygous mutants. Fish were screened via HRM analysis, followed by Sanger sequencing.

For *in vivo* mitochondrial Ca^{2+} imaging experiments *tmbim5*$^{-/-}$ fish were outcrossed with Tg(*HuC:CEPIA2mt*) zebrafish (obtained as a kind gift from prof. Jacek Kuźnicki laboratory). Their offspring were sorted for CEPIA2mt signal in the brain under the fluoroscope between 2 to 4 dpf.

Quantitative Real-Time PCR

Total RNA was extracted using TRI Reagent (Invitrogen, Cat# AM9738) according to a previously published protocol (Peterson & Freeman, 2009). Thirty embryos or larvae or organs dissected from two adult zebrafish were pooled together to obtain one RNA sample. RNA quality was verified by measuring absorbance at 260, 280, and 230 nm. Only samples with absorbance >1.8 at A260/280 nm were used for further processing. 500 ng of RNA was used for cDNA synthesis with iScript™ cDNA Synthesis Kit (BioRad, Cat# 1708891).

qRT-PCR was performed in duplicate using 25 ng of cDNA, SsoAdvanced Universal SYBR Green Supermix (BioRad, Cat# 1725274) and 0.25 µM of each primer. The primers that were used for qRT-PCR are listed in Table 1. Gene expression levels were analyzed using the CFX Connect Real-time PCR Detection System (Bio-Rad). Fold changes were calculated using the ΔΔCq method. *Eukaryotic translation elongation factor 1 α1, like 1* (*ef1a*) and *ribosomal protein L13a* (*rpl13a*) or *18S ribosomal RNA* (*18S*) (for *tmbim5* and *slc8b1* expression analysis during the development) were used as housekeeping genes for normalization. Changes in expression are expressed as fold changes using expression in WT as a reference value. The calculations were performed in Microsoft Excel.

Gene name	Abbreviation	Primer sequence	
		Forward	Reverse
transmembrane BAX inhibitor motif-containing protein 5 (growth hormone inducible transmembrane protein)	*tmbim5 (ghitm)*	GTCTCGGCATGTCCAGTGAG	CATGATCCCCATGAGCACCG
mitochondrial calcium uniporter	*mcu*	GTATCCCGCATTCGGTGTCT	CTGTTCTCAGACCGTGTGCT
mitochondrial calcium uptake 1	*micu1*	GACGGAGAGGTTGACCTTGA	GCGATCTCGGTGTCTCATCC
mitochondrial calcium uptake 2	*micu2*	ACCAAAGCAGACTTGGACGAA	GATCAACCCCTTGTCACCGA
mitochondrial calcium uptake family, member 3a	*micu3a*	TGCCGTTCCATTGGACAAGA	TGGTGTTAACCAGGTGTCGG
EF-Hand Domain Family Member D1	*efhd1*	ATCGACGTGTCCACTGAAGG	TCAGCCTCGAACTTACTGCG
leucine zipper-EF-hand containing transmembrane protein 1	*letm1*	GGTGGATGCAGAACACGCT	TCGCTCAGCATGTCAATCTCC
leucine zipper-EF-hand containing transmembrane protein 2	*letm2*	CCGATCTGACACCATACCCG	TCAGGCGTCCTGTCGAAAAA
solute carrier family 8 member B1	*slc8b1*	CGGAGTTCACACGGACCTAC	GATGGCTAGGGGCAGAAGAC
eukaryotic translation elongation factor 1 α1, like 1	*ef1a*	AAAATCGGTGGTGCTGGCAA	GGAACGGTGTGATTGAGGGA
transmembrane Protein 65	*tmem65*	CAACGCCATTCCCTTCATCG	TTCAATCTGAGTGCCAGCGG
solute carrier family 25 member 28 (mitoferrin-2)	*slc25a28*	ACCGGACTATGAGGGTTTGC	AGGCTCTGCATACGTGTCTTT
ribosomal protein L13a	*rpl13a*	TCTGGAGGACTGTAAGAGGTATGC	AGACGCACAATCTTGAGAGCAG
18S ribosomal RNA	*18S*	TCGCTAGTTGGCATCGTTTATG	CGGAGGTTCGAAGACGATCA
mitochondrial NADH dehydrogenase 1	*mt-nd1*	AGCCATCTCAAGCCTAGCAG	ATTGTTTGCGCTACAGCTCG

Table 1. Primers that were used for qRT-PCR
All primers' sequences are listed as from 5' to 3'.

Quantification of mitochondrial (mtDNA) to nuclear DNA (nDNA) ratio

DNA was isolated from zebrafish following a previously published protocol (Otten *et al*, 2020). Thirty 5-dpf larvae or one adult zebrafish were euthanized with tricaine (MS-222) and sacrificed to obtain a single DNA sample. The samples were incubated in lysis buffer (75 mM NaCl, 50 mM EDTA, 20 mM HEPES pH 7.5, 0.4% SDS, 1 mg/ml proteinase K) for at least 4 h in 55°C. For adult zebrafish, brain and skeletal muscle samples were dissected and homogenized with a plastic pestle in lysis buffer before incubation. DNA was precipitated with isopropanol and incubated for at least 6 h in -20°C. Following centrifugation, the DNA

pellet was washed with 70% ethanol, air-dried, and dissolved in Tris-EDTA (TE) buffer. Relative mitochondrial DNA (mtDNA) abundance was quantified by measuring the levels of *mitochondrial NADH dehydrogenase* (*mt-nd1*) and *nuclear elongation factor 1-alpha* (*ef1a*) using qRT-PCR (primers listed in Table 1). A total of 25 ng of DNA was used per qRT-PCR reaction. Changes in the mtDNA-to-nDNA ratio were calculated as fold changes using WT as a reference. Calculations were performed in Microsoft Excel.

Whole-mount in situ hybridization (WISH)

Riboprobes for the genes of interest were obtained by PCR using specific primers with T7 overlap at 5' end of reverse: *tmbim5 ISH forward*: 5'-CGCTGCTCAGAGGTGAAGGT-3', *tmbim5 ISH reverse*: 5'-taatacgactcactatagggATGTGTGCGGCATCTCTGCG-3', *slc8b1 ISH forward*: 5'-GTGTAGACGTGCGTTCTTGC-3', *slc8b1 ISH reverse*: 5'-taatacgactcactatagGG ACGAGACGCCACAGTAAA-3'. Purified PCR products were next utilized in *in vitro* transcription using MegaScript T7 Transcription Kit (Invitrogen, Cat# A57622) and digoxigenin (DIG)-labeled UTP (Roche, Cat# 11277073910) according to the manufacturer's instructions.

Zebrafish larvae were fixed in 4% paraformaldehyde (PFA; Sigma-Aldrich, P6148) in phosphate buffer saline (PBS) overnight at room temperature and stored at -20°C in the methanol. WISH was performed as previously described (Soman *et al*, 2019a) with several modifications. Briefly, after gradual rehydration with PBST (0.1% Tween-20 in PBS), permeabilization with 0.1% sodium citrate and 0.1% Triton X-100 for 10 min on ice, pre-hybridization in Hybridization Solution (HS; 50% deionized formamide, 5X sodium citrate buffer (SSC), 500 µg/ml tRNA, 50 µg/ml heparin, 0.1% Tween-20, 10mM citric acid, 5% sodium dextran sulfate) at 65°C for 3 h, the probes against target mRNAs were added in HS (0.5-3 µg probe/ml buffer) and incubated overnight at 67°C in the water bath. Next, larvae were washed with Hybridization Wash Solution (HWS; 50% deionized formamide, 5X SSC, 0.1% Tween-20, 10 mM citric acid) and subsequently with 75% HWS, 50% HWS, 25% HWS in 2X SSCT (SSC with 0.1% Tween-20) and 0.2X SSCT at 65°C. After blocking with 10% Blocking Reagent (Roche, Cat# 11096176001) in Maleic Acid buffer (100 mM maleic acid, 100 mM NaCl, 50 mM $MgCl_2$, 0.1% Tween-20) an alkaline phosphatase-conjugated anti-DIG antibody (Roche, Cat# 11093274910) was added to the blocking solution in 1:5000 dilution and incubated overnight at 4°C. Signal was developed by incubation with nitro-blue tetrazolium chloride (0.45 mg/ml, Roche, Cat# 11383213001) and 5-bromo-4-chloro-3-indolyl-phosphate (0.175 mg/ml, Roche, Cat# 11383221001) in Detection buffer (50 mM Tris-HCl pH 9.5, 50 mM NaCl, 25 mM $MgCl_2$, 0.05% Tween 20, 2% polyvinyl alcohol) for 3 h. Background signal was cleaned by 10 min wash with 100% methanol and samples were re-fixed with 4% PFA for 20 min at room temperature and stored in the glycerol until imaging. Imaging was performed using the Nikon SMZ25 stereomicroscope.

Histology

Adult eight-month-old zebrafish were fixed in Bouin's solution, dehydrated in ethanol, xylene and embedded in paraffin. 6 µm thick longitudinal and transverse sections were cut with a Leica microtome (RM2265, Leica) and stained with standard hematoxylin and eosin (H&E). For the determination of glycogen content and mucopolysaccharides accumulation, combined Alcian blue and periodic acid-Schiff (AB/PAS) reactions were performed. The structure of the muscle and connective tissue was visualized using Masson's trichrome stain. Microscopic analysis was carried out using a Nikon Eclipse 90i microscope with a Nikon DS5-U1 camera (Nikon Corporation, Japan) and the computer image analysis system NIS-Elements AR (Nikon Corporation, Japan). The quantification of Alcian Blue and

Masson's trichrome staining intensity and area was performed using the Colour Deconvolution plug-in in ImageJ.

Glycogen levels quantification

Glycogen levels in the muscles and liver of adult (1.5-year-old) zebrafish were quantified using a colorimetric glycogen assay (Abcam, Cat# ab169558) according to the manufacturer's instructions. Briefly, the assay is based on glycogen hydrolysis into glucose, which is oxidized to form an intermediate that reduces a colorless probe to a colored product with strong absorbance at 450 nm. Fish were euthanized with tricaine and dissected to obtain liver and muscle samples. Tissue was weighed before homogenization using a glass-Teflon homogenizer on ice. Glycogen levels were estimated by measuring optical density (OD) at 450 nm using an absorbance microplate reader (Tecan Sunrise). Samples not treated with the glycogen-hydrolyzing enzyme served as background controls. Glycogen content was normalized to tissue weight and expressed as fold change using WT as a reference.

Tetramethylrhodamine ethyl ester (TMRE) microinjections

The stock solution of TMRE (Invitrogen™, Cat# T669) was prepared by dissolving in dimethyl sulfoxide (DMSO, Sigma-Aldrich, Cat# D8418) to a final concentration of 10 mM. Injection solution was prepared at the day of the experiment by diluting 1:5 stock solution in the water (final concentration: 2 mM) and 1 nl was injected into the yolk of embryos at 1-2 cell stage. Microinjections were performed the same as during generation of *nclx*$^{-/-}$ mutants. Embryos were then grown according to standard methods described in the "Animal maintenance" section, but kept in the dark.

***In vivo* imaging with lightsheet fluorescence microscopy (LSFM)**

Stained or transgenic larvae were anesthetized with 0.2 mg/ml Tricaine (Sigma, Cat# A-5040), mounted in 2% low-melting-point agarose (Sigma-Aldrich, Cat# A9414) in a glass capillary and imaged under Zeiss Lightsheet Z.1 microscope using 40X objective (Zeiss) with excitation at 488 nm (AO and *Tg(CEPIA2mt)*) or 561 nm (TMRE). Fish were imaged from the dorsal side of the head and were pushed from capillary to be submerged in the medium from the top of the head up to the middle of the swimming bladder. Measurements were performed at room temperature.

Images were firstly processed in ZEN software (Zeiss) in order to obtain merged maximum projection images, exported to TIF files and analyzed further with ImageJ.

Cell death estimation by Acridine Orange in vivo staining: Acridine Orange (AO; Sigma-Aldrich, Cat# A8097) was added into the plates containing live 4 dpf zebrafish larvae (final concentration: 10 µg/ml E3). After 1 hour of incubation in the dark, the medium was exchanged to fresh E3 six times during 30 min. Z-stacks encompassing 45 µm of optic tectum with 5 µm interval were acquired with Zeiss Lightsheet Z.1 microscope. The counting of the AO-stained cells in the optic tectum of each larvae, that were considered as dying (Pyati *et al*, 2011), was performed manually on the maximum projection images with the CellCounter plug-in in the ImageJ. The number of cells was normalized to the analyzed area of the optic tectum.

Mitochondrial Ca^{2+} flux in the brain of alive zebrafish: In order to estimate mitochondrial Ca^{2+} content 5 dpf larvae, that expressed CEPIA2mt, Ca^{2+} probe targeted to the mitochondria under neural promoter HuC, were treated with 10 µM CCCP (Sigma-Aldrich, Cat# C2759) to induce depolarization of mitochondria and release of mitochondrial Ca^{2+}. After mounting the zebrafish larvae in the microscopic chamber filled with E3 the medium in the chamber was

exchanged to E3 with 10 µM CCCP (Sigma-Aldrich, Cat# C2759). To gain complete depolarization, larvae were treated for 10 min. Z-stacks encompassing 10 µm of optic tectum with 1 µm interval were acquired with Zeiss Lightsheet Z.1 microscope every 5 s during 10 min of treatment.

During image analysis The StackReg plug-in was applied for movement correction. Mitochondria were detected by thresholding and mean fluorescence for mitochondria in the selected square ROI in the optic tectum was calculated. Background fluorescence was calculated as the mean fluorescence of a square that was localized besides the fish, and subtracted from the mean fluorescence of ROI value: $F = F_{ROI} - F_{background}$. F was normalized by the value obtained after full depolarization (F/F_{CCCP}) and the ratio between basal fluorescence (F_0) and F_{CCCP} was calculated to compare mitochondrial Ca^{2+} content between variants similarly to the method described in (Stavsky *et al*, 2021).

Mitochondrial membrane potential (MMP) in vivo measurements: Two days after microinjections with TMRE dechorionated larvae were imaged using LSFM as described above. 2 dpf larvae were treated with 10 µM CCCP (Sigma-Aldrich, Cat# C2759) to induce depolarization of mitochondria. To gain complete depolarization, larvae were treated for 5 min, due to higher toxicity of CCCP treatment at this stage than at 5 dpf. Z-stacks encompassing 10 µm of optic tectum with 1 µm interval were acquired with Zeiss Lightsheet Z.1 microscope every 5 s during 5 min of treatment. F was normalized by the value obtained after full depolarization (F/F_{CCCP}) and the ratio between basal fluorescence (F_0) and F_{CCCP} was calculated to compare mitochondrial membrane potential between variants. Image analysis was performed as for mitochondrial Ca^{2+} measurements described above.

Isolation zebrafish larvae mitochondria

To obtain functional mitochondria from zebrafish 5 dpf larvae a modified method described in (Prudent *et al*, 2013) was used. Larvae (300 - 450 per genotype) were sacrificed by Tricaine treatment and washed with the ice-cold Ringer's buffer (1.8 mM $CaCl_2$, 116 mM NaCl, 2.9 mM KCl, 5 mM HEPES, pH 7.5). Next, rinsed larvae were incubated on ice in the mitochondria isolation buffer (MIB, 210 mM mannitol, 70 mM sucrose, 1mM EDTA, 10mM HEPES, pH 7.5) supplemented with 2 mM PMSF just before usage and transferred to precooled glass-teflon homogenizer in MIB with 2 mM PMSF and BSA (2 mg/ml). Zebrafish tissue was manually homogenized on ice with 50x strokes and centrifuged (1,500 x g, 10 min). Supernatant was transferred to a new tube and centrifuged again to eliminate nuclei and cell debris. After the high-speed centrifugation (14,000 x g, 15 min) of the obtained supernatant, the pellets containing the mitochondria were washed twice with 1 ml ice-cold KCl medium (125 mM KCl, 2 mM K_2HPO_4, 1 mM $MgCl_2$, 5 mM glutamate, 5 mM malic acid, 20 mM HEPES, pH 7). Pellet was gently resuspended with 0.1 µl of KCl medium per larvae and protein amount was established by Bradford protein assay. During the whole procedure samples were kept on the ice, all centrifugations steps were performed at 4°C and all used tubes and media were precooled on the ice.

Ca^{2+} measurements in mitochondria isolated from zebrafish larvae

Mitochondrial Ca^{2+} fluxes was measured in freshly isolated mitochondria from 5 dpf zebrafish larvae. 25 µg of mitochondria was gently suspended in KCl medium with glutamate (5 mM), malic acid (5 mM) added freshly and transferred into 96-well half-area black polystyrene microplate (Corning®, Cat# CLS3694). Thapsigargin (0.2 µM, Invitrogen™, Cat# T7459) was added in order to inhibit SERCA pump from potential contaminants from endoplasmic reticulum in the samples. The bath [Ca^{2+}] was detected using the Ca^{2+}-sensitive dye Oregon Green™ 488 BAPTA-5N hexapotassium salt (2 µM, Invitrogen™, Cat# O6812) as described

in (Soman *et al*, 2019a). The signal was measured using a plate reader (Tecan Infinite M1000 Pro) at Ex/Em 494/521 nm. Measurements were performed at room temperature.

For the analysis, the first read-out of baseline recording was defined as F_0 and used for normalization. All traces are shown as $\Delta F/F_0$, where $\Delta F = F - F_0$.

Mitochondrial Ca^{2+} uptake assay: 20 µM $CaCl_2$ diluted in KCl medium was added with a multichannel pipette after 30 s of baseline recording. Signal was measured every 3 s for 10 min. Ca^{2+} uptake was calculated as the difference between maximal $\Delta F/F_0$ (first read-out after $CaCl_2$ addition) and $\Delta F/F_0$ value measured 2 min after $CaCl_2$ addition. Mitochondria Ca^{2+} level: Mitochondrial Ca^{2+} levels were estimated by measuring the amount of Ca^{2+} released from mitochondria following complete depolarization with CCCP. A 10 µM CCCP solution diluted in KCl medium was added using a multichannel pipette after 30 seconds of baseline recording. Simultaneously, KCl medium without CCCP was added to negative control samples. Fluorescence signals were recorded every 5 seconds for 5 minutes. Mitochondrial Ca^{2+} levels were quantified as the maximum $\Delta F/F_0$ value observed after CCCP addition.

Na^+-dependent mitochondrial Ca^{2+} efflux: Mitochondria were first loaded with 20 µM $CaCl_2$ diluted in KCl medium, as described for the mitochondrial uptake assay. Next, mitochondrial Ca^{2+} uptake via MCU was inhibited by adding 10 µM Ru360 (Sigma-Aldrich, Cat# 557440). To estimate the amount of Na^+-independent Ca^{2+} efflux following Ru360 addition, the last $\Delta F/F_0$ value recorded after $CaCl_2$ addition was subtracted from the maximum $\Delta F/F_0$ value obtained after Ru360 addition. Subsequently, Na^+-dependent mitochondrial Ca^{2+} efflux was stimulated by adding 10 mM NaCl (KCl medium in which 120 mM K^+ was substituted with Na^+). To estimate the amount of Ca^{2+} efflux following Na^+ addition, the last $\Delta F/F_0$ value recorded after Ru360 addition was subtracted from the maximum $\Delta F/F_0$ value after Na^+ addition. Fluorescence signals were recorded every 5 seconds for 5 minutes following each treatment.

In experiments testing the impact of CGP-37157 on Na^+-dependent Ca^{2+} efflux, mitochondria were pretreated with 10 µM CGP-37157 (Sigma-Aldrich, Cat# 220005) 10 minutes before and during the recording.

Behavioral analysis

Coiling activity of zebrafish embryos: Randomly selected embryos were transferred to a 12-well plate (4 embryos/well) in 2 ml of E3 and acclimated for 2h in 28ºC. Coiling activity was recorded 30 hpf using the Nikon SMZ25 stereomicroscope for 3 min with 10 frames /s acquisition rate. The number of coiling events for each embryo was counted manually.

Open field test: Randomly selected 4 dpf larvae were acclimated to the behavioral testing room for at least 15 min. Two minutes before recording locomotor activity, the larvae were transferred to a 12-well plate that was then placed in the ZebraBox, a high-throughput monitoring system (ViewPoint). The experiment was performed in a volume of 2 mL of E3 medium, and the light intensity was set to 70%. Locomotor activity was recorded for 10 min.

Visual motor response: The experiment was performed according to the procedure described previously (Kedra *et al*, 2020). On the day before the experiment, the larvae were placed in 24-well plates that contained 0.5 mL of E3 medium. Thirty minutes before recording locomotor activity, the plates were placed in the ZebraBox. The experiment consisted of three phases of the following changes in lighting conditions: baseline (0–10 min, 0% light intensity), light (10–20 min, 70% light intensity), and dark (20–30 min, 0% light intensity).

Novel tank test for adult zebrafish: The 8-months-old zebrafish were acclimated to the behavioral testing room for one week before the experiment. Fish were placed individually in a transparent tank (24 cm length x 14 cm height x 6cm width) filled with aquarium water. ZebraCube, an adult fish monitoring system (ViewPoint) was utilized to record animals' behavior for 15 min.

The video files acquired during experiments with larvae and adult zebrafish were further analyzed using EthoVision XT software (Noldus).

Transmission electron microscopy of zebrafish larvae

Zebrafish larvae at 5 dpf were euthanized with Tricane. The animals were fixed in 2.5% glutaraldehyde for 24 hours at 4°C, washed in PBS, postfixed in 1% osmium tetroxide for 1 hour, washed with water, and stained with 1% aqueous uranyl acetate overnight at 4°C. The larvae were dehydrated and infiltrated with epoxy resin (Sigma Aldrich, Cat# 45-359-1EA-F). Samples were then polymerised at 60°C for 48 hours. Polymerized blocks were trimmed with a tissue processor (Leica EM TP) and cut with an ultramicrotome (EM UC7, Leica) to obtain ultrathin sections (70 nm thick), which were collected on nickel grids (200 mesh, Agar Scientific, Cat# G2200N). The grids were examined using a Tecnai T12 BioTwin transmission electron microscope (FEI) equipped with a 16-megapixel TemCam-F416 camera (TVIPS GmbH) at the Microscopy and Cytometry Facility at IIMCB in Warsaw.

Statistical analysis

All statistical analyses were conducted using R version 4.1.2. Box and whisker plots were generated with R, while other graphs were generated with Microsoft Excel or GaphPad Prism version 8. All datasets were tested for outliers using a Grubbs's test and for normal distribution using the Shapiro-Wilk test. The applied statistical tests are indicated in the figure legends.

Acknowledgments

We thank the Laboratory of Neurodegeneration at IIMCB and specifically Prof. Jacek Kuznicki for providing laboratory space to conduct research on zebrafish, *mcu*$^{-/-}$ and Tg(*CEPIA2mt*) zebrafish lines and helpful discussions. We acknowledge Michał Bazała and Dr Justyna Jędrychowska for generating the Tg(*CEPIA2mt*) zebrafish line. We thank Prof. Jacek Kuźnicki and Prof. Barbara Zabłocka for critical reading of the paper. We acknowledge the IIMCB Zebrafish Core Facility for service and fish material and Microscopy and Cytometry Facility for providing access to LSFM. This research was funded by the National Science Centre, Poland (021/40/C/NZ4/00031) to I.W.

Author contributions

I.W. designed and performed most of the experiments with contributions from S.B. and Ł.M., D.A-U. performed histological analysis of adult zebrafish, M.M. and A.S. performed TEM analysis of larvae mitochondria, A.M. supervised experiments, I.W analyzed data and interpreted results, I.W. and A.M. wrote the manuscript.

Disclosure and competing interests statement

The authors declare no competing interest.

Data availability

This study includes no data deposited in external repositories. No unbiased larger data sets were generated in this study. All data are presented in the results or as supplemental data.

References

Altschuld RA, Hohl CM, Castillo LC, Garleb AA, Starling RC & Brierley GP (1992) Cyclosporin inhibits mitochondrial calcium efflux in isolated adult rat ventricular cardiomyocytes. *Am J Physiol* 262: H1699–704

Austin S, Mekis R, Mohammed SEM, Scalise M, Wang W-A, Galluccio M, Pfeiffer C, Borovec T, Parapatics K, Vitko D, *et al* (2022) TMBIM5 is the Ca2+ /H+ antiporter of mammalian mitochondria. *EMBO Rep* 23: e54978

Austin S, Tavakoli M, Pfeiffer C, Seifert J, Mattarei A, De Stefani D, Zoratti M & Nowikovsky K (2017) LETM1-Mediated K and Na Homeostasis Regulates Mitochondrial Ca Efflux. *Front Physiol* 8: 839

Baughman JM, Perocchi F, Girgis HS, Plovanich M, Belcher-Timme CA, Sancak Y, Bao XR, Strittmatter L, Goldberger O, Bogorad RL, *et al* (2011) Integrative genomics identifies MCU as an essential component of the mitochondrial calcium uniporter. *Nature* 476: 341–345

Bernardi P, Gerle C, Halestrap AP, Jonas EA, Karch J, Mnatsakanyan N, Pavlov E, Sheu S-S & Soukas AA (2023) Identity, structure, and function of the mitochondrial permeability transition pore: controversies, consensus, recent advances, and future directions. *Cell Death Differ* 30: 1869–1885

Bisbach CM, Hutto RA, Poria D, Cleghorn WM, Abbas F, Vinberg F, Kefalov VJ, Hurley JB & Brockerhoff SE (2020) Mitochondrial Calcium Uniporter (MCU) deficiency reveals an alternate path for Ca uptake in photoreceptor mitochondria. *Sci Rep* 10: 16041

Bitarafan F, Khodaeian M, Amjadi Sardehaei E, Darvishi FZ, Almadani N, Nilipour Y & Garshasbi M (2021) Identification of a novel MICU1 nonsense variant causes myopathy with extrapyramidal signs in an Iranian consanguineous family. *Mol Cell Pediatr* 8: 6

Bultynck G, Kiviluoto S & Methner A (2014) Bax inhibitor-1 is likely a pH-sensitive calcium leak channel, not a H+/Ca2+ exchanger. *Sci Signal* 7: e22

Control of muscle fibre-type diversity during embryonic development: The zebrafish paradigm (2013) *Mechanisms of Development* 130: 447–457

Debattisti V, Horn A, Singh R, Seifert EL, Hogarth MW, Mazala DA, Huang KT, Horvath R, Jaiswal JK & Hajnóczky G (2019) Dysregulation of Mitochondrial Ca Uptake and Sarcolemma Repair Underlie Muscle Weakness and Wasting in Patients and Mice Lacking MICU1. *Cell Rep* 29: 1274–1286.e6

Delgado de la Herran H, Vecellio Reane D, Cheng Y, Katona M, Hosp F, Greotti E, Wettmarshausen J, Patron M, Mohr H, Prudente de Mello N, *et al* (2024) Systematic mapping of mitochondrial calcium uniporter channel (MCUC)-mediated calcium signaling networks. *EMBO J*

De Stefani D, Raffaello A, Teardo E, Szabò I & Rizzuto R (2011) A forty-kilodalton protein of the inner membrane is the mitochondrial calcium uniporter. *Nature* 476: 336–340

Garbincius JF, Salik O, Cohen HM, Choya-Foces C, Mangold AS, Makhoul AD, Schmidt AE, Khalil DY, Doolittle JJ, Wilkinson AS, *et al* (2023) TMEM65 regulates NCLX-dependent mitochondrial calcium efflux. *bioRxiv*

Gasanov EV, Jędrychowska J, Pastor M, Wiweger M, Methner A & Korzh VP (2021) An

improved method for precise genome editing in zebrafish using CRISPR-Cas9 technique. *Mol Biol Rep* 48: 1951–1957

Gherardi G, Nogara L, Ciciliot S, Fadini GP, Blaauw B, Braghetta P, Bonaldo P, De Stefani D, Rizzuto R & Mammucari C (2019) Loss of mitochondrial calcium uniporter rewires skeletal muscle metabolism and substrate preference. *Cell Death Differ* 26: 362–381

Hasumura T & Meguro S (2016) Exercise quantity-dependent muscle hypertrophy in adult zebrafish (Danio rerio). *J Comp Physiol B* 186: 603–614

Jiang D, Zhao L & Clapham DE (2009) Genome-wide RNAi screen identifies Letm1 as a mitochondrial Ca2+/H+ antiporter. *Science* 326: 144–147

Kedra M, Banasiak K, Kisielewska K, Wolinska-Niziol L, Jaworski J & Zmorzynska J (2020) TrkB hyperactivity contributes to brain dysconnectivity, epileptogenesis, and anxiety in zebrafish model of Tuberous Sclerosis Complex. *Proc Natl Acad Sci U S A* 117: 2170–2179

Kettunen P (2020) Calcium Imaging in the Zebrafish. *Adv Exp Med Biol* 1131: 901–942

Kilkenny C, Browne WJ, Cuthill IC, Emerson M & Altman DG (2010) Improving bioscience research reporting: the ARRIVE guidelines for reporting animal research. *PLoS Biol* 8: e1000412

König T, Tröder SE, Bakka K, Korwitz A, Richter-Dennerlein R, Lampe PA, Patron M, Mühlmeister M, Guerrero-Castillo S, Brandt U, *et al* (2016) The m-AAA Protease Associated with Neurodegeneration Limits MCU Activity in Mitochondria. *Mol Cell* 64: 148–162

Labun K, Montague TG, Krause M, Torres Cleuren YN, Tjeldnes H & Valen E (2019) CHOPCHOP v3: expanding the CRISPR web toolbox beyond genome editing. *Nucleic Acids Res* 47: W171–W174

Langenbacher AD, Shimizu H, Hsu W, Zhao Y, Borges A, Koehler C & Chen J-N (2020) Mitochondrial Calcium Uniporter Deficiency in Zebrafish Causes Cardiomyopathy With Arrhythmia. *Front Physiol* 11: 617492

Lessman CA & Carver EA (2014) Zebrafish: Topics in Reproduction, Toxicology and Development Nova Science Publishers

Lewis-Smith D, Kamer KJ, Griffin H, Childs A-M, Pysden K, Titov D, Duff J, Pyle A, Taylor RW, Yu-Wai-Man P, *et al* (2016) Homozygous deletion in MICU1 presenting with fatigue and lethargy in childhood. *Neurol Genet* 2: e59

Liu JC, Liu J, Holmström KM, Menazza S, Parks RJ, Fergusson MM, Yu Z-X, Springer DA, Halsey C, Liu C, *et al* (2016) MICU1 Serves as a Molecular Gatekeeper to Prevent In Vivo Mitochondrial Calcium Overload. *Cell Rep* 16: 1561–1573

Logan CV, Szabadkai G, Sharpe JA, Parry DA, Torelli S, Childs A-M, Kriek M, Phadke R, Johnson CA, Roberts NY, *et al* (2014) Loss-of-function mutations in MICU1 cause a brain and muscle disorder linked to primary alterations in mitochondrial calcium signaling. *Nat Genet* 46: 188–193

Luongo TS, Lambert JP, Gross P, Nwokedi M, Lombardi AA, Shanmughapriya S, Carpenter AC, Kolmetzky D, Gao E, van Berlo JH, *et al* (2017) The mitochondrial Na+/Ca2+ exchanger is essential for Ca2+ homeostasis and viability. *Nature* 545: 93–97

Mallilankaraman K, Cárdenas C, Doonan PJ, Chandramoorthy HC, Irrinki KM, Golenár T, Csordás G, Madireddi P, Yang J, Müller M, *et al* (2012a) MCUR1 is an essential component of mitochondrial Ca2+ uptake that regulates cellular metabolism. *Nat Cell Biol* 14: 1336–1343

Mallilankaraman K, Doonan P, Cárdenas C, Chandramoorthy HC, Müller M, Miller R, Hoffman NE, Gandhirajan RK, Molgó J, Birnbaum MJ, *et al* (2012b) MICU1 is an essential gatekeeper for MCU-mediated mitochondrial Ca(2+) uptake that regulates cell survival. *Cell* 151: 630–644

Mammucari C, Gherardi G, Zamparo I, Raffaello A, Boncompagni S, Chemello F, Cagnin S, Braga A, Zanin S, Pallafacchina G, *et al* (2015) The mitochondrial calcium uniporter controls skeletal muscle trophism in vivo. *Cell Rep* 10: 1269–1279

Mandal A, Pinter K & Drerup CM (2018) Analyzing Neuronal Mitochondria in vivo Using Fluorescent Reporters in Zebrafish. *Front Cell Dev Biol* 6: 414920

Matthews M, Trevarrow B & Matthews J (2002) A virtual tour of the Guide for zebrafish users. *Lab Anim* 31: 34–40

Meng K, Hu Y, Wang D, Li Y, Shi F, Lu J, Wang Y, Cao Y, Zhang CZ & He Q-Y (2023) EFHD1, a novel mitochondrial regulator of tumor metastasis in clear cell renal cell carcinoma. *Cancer Sci* 114: 2029–2040

Metcalfe WK, Kimmel CB & Schabtach E (1985) Anatomy of the posterior lateral line system in young larvae of the zebrafish. *J Comp Neurol* 233: 377–389

Moreno-Mateos MA, Vejnar CE, Beaudoin J-D, Fernandez JP, Mis EK, Khokha MK & Giraldez AJ (2015) CRISPRscan: designing highly efficient sgRNAs for CRISPR-Cas9 targeting in vivo. *Nat Methods* 12: 982–988

Murphy E, Pan X, Nguyen T, Liu J, Holmström KM & Finkel T (2014) Unresolved questions from the analysis of mice lacking MCU expression. *Biochem Biophys Res Commun* 449: 384–385

Nowikovsky K, Froschauer EM, Zsurka G, Samaj J, Reipert S, Kolisek M, Wiesenberger G & Schweyen RJ (2004) The LETM1/YOL027 gene family encodes a factor of the mitochondrial K+ homeostasis with a potential role in the Wolf-Hirschhorn syndrome. *J Biol Chem* 279: 30307–30315

Oka T, Sayano T, Tamai S, Yokota S, Kato H, Fujii G & Mihara K (2008) Identification of a novel protein MICS1 that is involved in maintenance of mitochondrial morphology and apoptotic release of cytochrome c. *Mol Biol Cell* 19: 2597–2608

Orrenius S, Gogvadze V & Zhivotovsky B (2015) Calcium and mitochondria in the regulation of cell death. *Biochem Biophys Res Commun* 460: 72–81

Otten ABC, Kamps R, Lindsey P, Gerards M, Pendeville-Samain H, Muller M, van Tienen FHJ & Smeets HJM (2020) Tfam Knockdown Results in Reduction of mtDNA Copy Number, OXPHOS Deficiency and Abnormalities in Zebrafish Embryos. *Front Cell Dev Biol* 8: 521612

Palty R, Silverman WF, Hershfinkel M, Caporale T, Sensi SL, Parnis J, Nolte C, Fishman D, Shoshan-Barmatz V, Herrmann S, *et al* (2010) NCLX is an essential component of mitochondrial Na+/Ca2+ exchange. *Proc Natl Acad Sci U S A* 107: 436–441

Pan X, Liu J, Nguyen T, Liu C, Sun J, Teng Y, Fergusson MM, Rovira II, Allen M, Springer DA, *et al* (2013) The physiological role of mitochondrial calcium revealed by mice lacking the mitochondrial calcium uniporter. *Nat Cell Biol* 15: 1464–1472

Patron M, Checchetto V, Raffaello A, Teardo E, Vecellio Reane D, Mantoan M, Granatiero V, Szabò I, De Stefani D & Rizzuto R (2014) MICU1 and MICU2 finely tune the mitochondrial Ca2+ uniporter by exerting opposite effects on MCU activity. *Mol Cell* 53: 726–737

Patron M, Tarasenko D, Nolte H, Kroczek L, Ghosh M, Ohba Y, Lasarzewski Y, Ahmadi ZA, Cabrera-Orefice A, Eyiama A, *et al* (2022) Regulation of mitochondrial proteostasis by the proton gradient. *EMBO J* 41: e110476

Peterson SM & Freeman JL (2009) RNA isolation from embryonic zebrafish and cDNA synthesis for gene expression analysis. *J Vis Exp*

Prudent J, Popgeorgiev N, Bonneau B, Thibaut J, Gadet R, Lopez J, Gonzalo P, Rimokh R, Manon S, Houart C, *et al* (2013) Bcl-wav and the mitochondrial calcium uniporter drive gastrula morphogenesis in zebrafish. *Nat Commun* 4: 2330

Pyati UJ, Gjini E, Carbonneau S, Lee J-S, Guo F, Jette CA, Kelsell DP & Look AT (2011) p63 mediates an apoptotic response to pharmacological and disease-related ER stress in the developing epidermis. *Dev Cell* 21: 492–505

Schneider CA, Rasband WS & Eliceiri KW (2012) NIH Image to ImageJ: 25 years of image analysis. *Nat Methods* 9: 671–675

Seitaj B, Maull F, Zhang L, Wüllner V, Wolf C, Schippers P, La Rovere R, Distler U, Tenzer S, Parys JB, *et al* (2020) Transmembrane BAX Inhibitor-1 Motif Containing Protein 5 (TMBIM5) Sustains Mitochondrial Structure, Shape, and Function by Impacting the Mitochondrial Protein Synthesis Machinery. *Cells* 9

Shao J, Fu Z, Ji Y, Guan X, Guo S, Ding Z, Yang X, Cong Y & Shen Y (2016) Leucine zipper-EF-hand containing transmembrane protein 1 (LETM1) forms a Ca/H antiporter. *Sci Rep* 6: 34174

Soman SK, Bazała M, Keatinge M, Bandmann O & Kuznicki J (2019a) Restriction of mitochondrial calcium overload by inactivation renders a neuroprotective effect in zebrafish models of Parkinson's disease. *Biol Open* 8

Soman SK, Bazała M, Keatinge M, Bandmann O & Kuznicki J (2019b) Restriction of mitochondrial calcium overload by inactivation renders a neuroprotective effect in zebrafish models of Parkinson's disease. *Biol Open* 8

Soman S, Keatinge M, Moein M, Da Costa M, Mortiboys H, Skupin A, Sugunan S, Bazala M, Kuznicki J & Bandmann O (2017) Inhibition of the mitochondrial calcium uniporter rescues dopaminergic neurons in pink1 zebrafish. *Eur J Neurosci* 45: 528–535

Stavsky A, Stoler O, Kostic M, Katoshevsky T, Assali EA, Savic I, Amitai Y, Prokisch H, Leiz S, Daumer-Haas C, *et al* (2021) Author Correction: Aberrant activity of mitochondrial NCLX is linked to impaired synaptic transmission and is associated with mental retardation. *Commun Biol* 4: 755

Suzuki J, Kanemaru K, Ishii K, Ohkura M, Okubo Y & Iino M (2014) Imaging intraorganellar Ca2+ at subcellular resolution using CEPIA. *Nat Commun* 5: 4153

Tomar D, Jaña F, Dong Z, Quinn WJ 3rd, Jadiya P, Breves SL, Daw CC, Srikantan S, Shanmughapriya S, Nemani N, *et al* (2019) Blockade of MCU-Mediated Ca Uptake Perturbs Lipid Metabolism via PP4-Dependent AMPK Dephosphorylation. *Cell Rep* 26: 3709–3725.e7

Tsai C-W, Wu Y, Pao P-C, Phillips CB, Williams C, Miller C, Ranaghan M & Tsai M-F (2017) Proteolytic control of the mitochondrial calcium uniporter complex. *Proc Natl Acad Sci U S A* 114: 4388–4393

Tsai M-F, Jiang D, Zhao L, Clapham D & Miller C (2014) Functional reconstitution of the mitochondrial Ca2+/H+ antiporter Letm1. *J Gen Physiol* 143: 67–73

Vais H, Mallilankaraman K, Mak D-OD, Hoff H, Payne R, Tanis JE & Foskett JK (2016) EMRE Is a Matrix Ca(2+) Sensor that Governs Gatekeeping of the Mitochondrial Ca(2+) Uniporter. *Cell Rep* 14: 403–410

Vais H, Tanis JE, Müller M, Payne R, Mallilankaraman K & Foskett JK (2015) MCUR1, CCDC90A, Is a Regulator of the Mitochondrial Calcium Uniporter. *Cell Metab* 22: 533–535

Vetralla M, Wischhof L, Cadenelli V, Scifo E, Ehninger D, Rizzuto R, Bano D & De Stefani D (2023) TMEM65-dependent Ca2+ extrusion safeguards mitochondrial homeostasis. *bioRxiv*: 2023.10.10.561661

Vicente M, Salgado-Almario J, Soriano J, Burgos M, Domingo B & Llopis J (2019) Visualization of Mitochondrial Ca Signals in Skeletal Muscle of Zebrafish Embryos with Bioluminescent Indicators. *Int J Mol Sci* 20

Wiweger M, Majewski L, Adamek-Urbanska D, Wasilewska I & Kuznicki J (2021) -Deficient Zebrafish Reproduce Neurological and Inflammatory Symptoms of Niemann-Pick Type C Disease. *Front Cell Neurosci* 15: 647860

Yu W, Zhang B, Song H, Zhan R, Li L, He C, Jiang Q, Wang X, Wei L, Zhao N, *et al* (2020) Preliminary investigation demonstrating the GHITM gene probably involved in apoptosis and growth of the golden apple snail (Pomacea canaliculata). *BMC Genomics* 21: 19

Zhang L, Dietsche F, Seitaj B, Rojas-Charry L, Latchman N, Tomar D, Wüst RC, Nickel A, Frauenknecht KB, Schoser B, *et al* (2022) TMBIM5 loss of function alters mitochondrial matrix ion homeostasis and causes a skeletal myopathy. *Life Sci Alliance* 5

Zhang Y, Reyes L, Sun J, Liu C, Springer D, Noguchi A, Aponte AM, Munasinghe J, Covian R, Murphy E, *et al* (2023) Loss of TMEM65 causes mitochondrial disease mediated by mitochondrial calcium. *bioRxiv*: 2022.08.02.502535

Extended view

Normal behavior of *tmbim5*$^{-/-}$ zebrafish

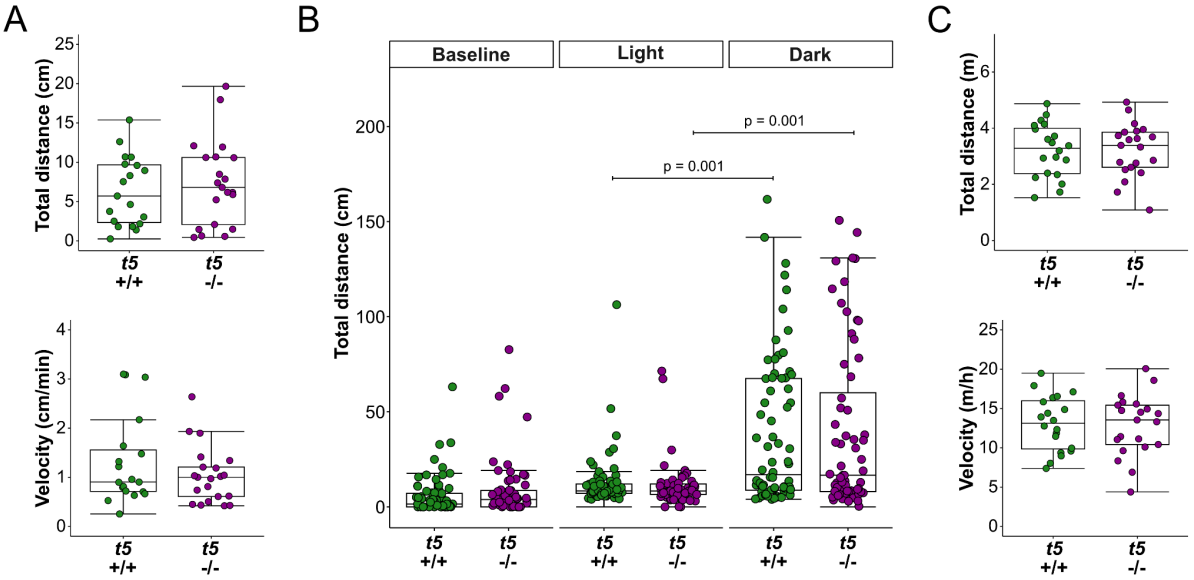

Figure EV1. Normal behavior of *tmbim5*$^{-/-}$ zebrafish.

A) Locomotor activity of 5 dpf larvae in an open-field test is not affected by *tmbim5* knockout (KO). Total distance traveled and mean velocity are plotted as box-and-whisker plots (box: 25th–75th percentile; whiskers: min to max), with each dot representing an individual larva (n = 19–21). Number of experiments = 3. Statistical analysis: *t*-test (total distance) or Mann–Whitney test (velocity).

B) Normal visual-motor response of 5 dpf *tmbim5*$^{-/-}$ larvae. Total distance covered during each phase of the experiment is plotted as box-and-whisker plots (box: 25th–75th percentile; whiskers: min to max), with each dot representing an individual larva (n = 64–72). Number of experiments = 3. Statistical analysis: Kruskal-Wallis test followed by Dunn's test.

C) Locomotor activity of adult (8-month-old) fish in a novel tank test is not affected by *tmbim5* KO. Total distance traveled and mean velocity are plotted as box-and-whisker plots (box: 25th–75th percentile; whiskers: min to max), with each dot representing an individual fish (n = 20–21). Number of experiments = 3. Statistical analysis: Mann–Whitney test.

Histology of brain, muscle and liver of adult *tmbim5*$^{-/-}$ fish

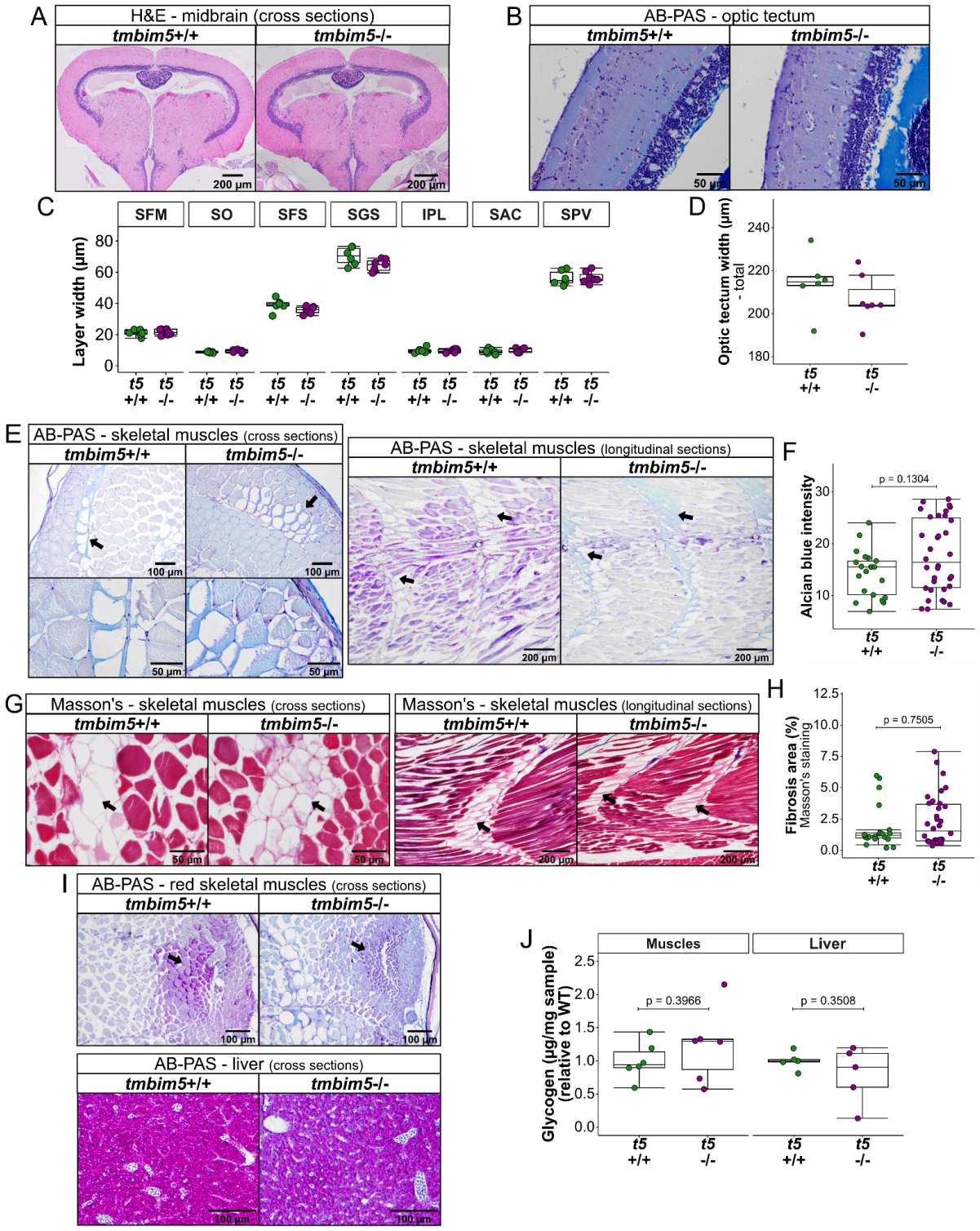

Figure EV2. Histology of brain, muscle and liver of adult *tmbim5*$^{-/-}$ fish

A-D) Normal histology of the *tmbim5*$^{-/-}$ fish brain. A) Representative images of cross-sections of the WT and *tmbim5*$^{-/-}$ midbrain stained with H&E. B) Representative images of cross-sections of the WT and *tmbim5*$^{-/-}$ optic tectum stained with AB-PAS. C) Quantification of the width of optic tectum layers. D) Comparison of total optic tectum width between WT and *tmbim5*$^{-/-}$ fish, showing no significant differences. Data are presented as box-and-whisker plots (box: 25th–75th percentile; whiskers: min to max), with each dot representing an individual fish (5–7 slices analyzed per fish, 5 measurements per slice, n = 6–7). Statistical analysis: *t*-test with BH correction for multiple comparisons. SFM – Stratum Fibrosum Superficiale, SO – Stratum Opticum, SFS – Stratum Fibrosum Superficiale, SGS – Stratum Fibrosum Griseum, IPL – Internal Plexiform Layer, SAC – Stratum Album Centrale, SPV – Stratum Periventriculare.

E-F) Enhanced Alcian Blue (AB) staining in the intermuscular spaces of *tmbim5*$^{-/-}$ fish. E) Representative images of cross- and longitudinal sections of WT and *tmbim5*$^{-/-}$ fish stained with AB-PAS (Periodic Acid-Schiff). Lower panels show magnified views of AB-stained intermuscular spaces (indicated by arrows). F) Quantification of AB staining intensity. Data are presented as box-and-whisker plots (box: 25th–75th percentile; whiskers: min to max), showing a trend toward increased staining intensity in *tmbim5*$^{-/-}$ fish. Each dot represents the average for one slice (n = 21–34, number of fish = 7). Statistical analysis: Mann–Whitney test.

G-H) Masson's trichrome staining of skeletal muscles reveals no differences in *tmbim5*$^{-/-}$ fish. G) Representative images of cross- and longitudinal sections of WT and *tmbim5*$^{-/-}$ fish. Intermuscular spaces that showed positive AB staining are marked with arrows. H) Quantification of Masson's trichrome-positive areas, showing no significant changes in *tmbim5*$^{-/-}$ fish. Each dot represents the average for one slice (n = 21–34, number of fish = 7). Statistical analysis: Mann–Whitney test.

I) Reduced PAS staining intensity in the muscle and liver of *tmbim5*$^{-/-}$ adult (8-month-old) fish. Representative images of cross-sections of WT and *tmbim5*$^{-/-}$ fish stained with AB-PAS.

J) Glycogen levels remain unchanged in the muscle and liver of *tmbim5*$^{-/-}$ adult (1.5-year-old) fish. Quantification was performed using a colorimetric glycogen assay (n = 5–6, number of experiments = 2). Statistical analysis: t-test.

Unchanged mitochondrial Ca^{2+} levels in the mitochondria isolated from tmbim5$^{-/-}$ larvae

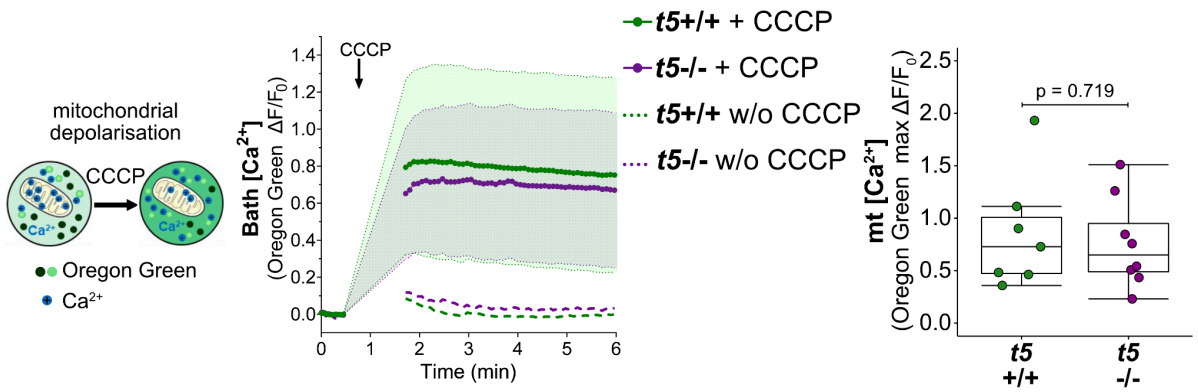

Figure EV3. Unchanged mitochondrial Ca^{2+} levels in the mitochondria isolated from *tmbim5*$^{-/-}$ larvae.

No alteration in mitochondrial Ca^{2+} levels was observed in isolated mitochondria. CCCP (10 μM) was used to depolarize mitochondria and induce Ca^{2+} efflux. Fluorescence was normalized to the initial value (F_0). Data are presented as mean ± SD $\Delta F/F_0$ traces. Mitochondria treated with a buffer without CCCP (w/o CCCP) served as negative controls. Maximal $\Delta F/F_0$ values were calculated and presented as box-and-whisker plots (box: 25th–75th percentile; whiskers: min to max), with each dot representing an independent biological replicate (n = 7–8). Statistical analysis: *t*-test.

Tmbim5 deficiency does not affect expression of genes encoding mitochondrial proteins involved in Ca^{2+} transport in zebrafish larvae

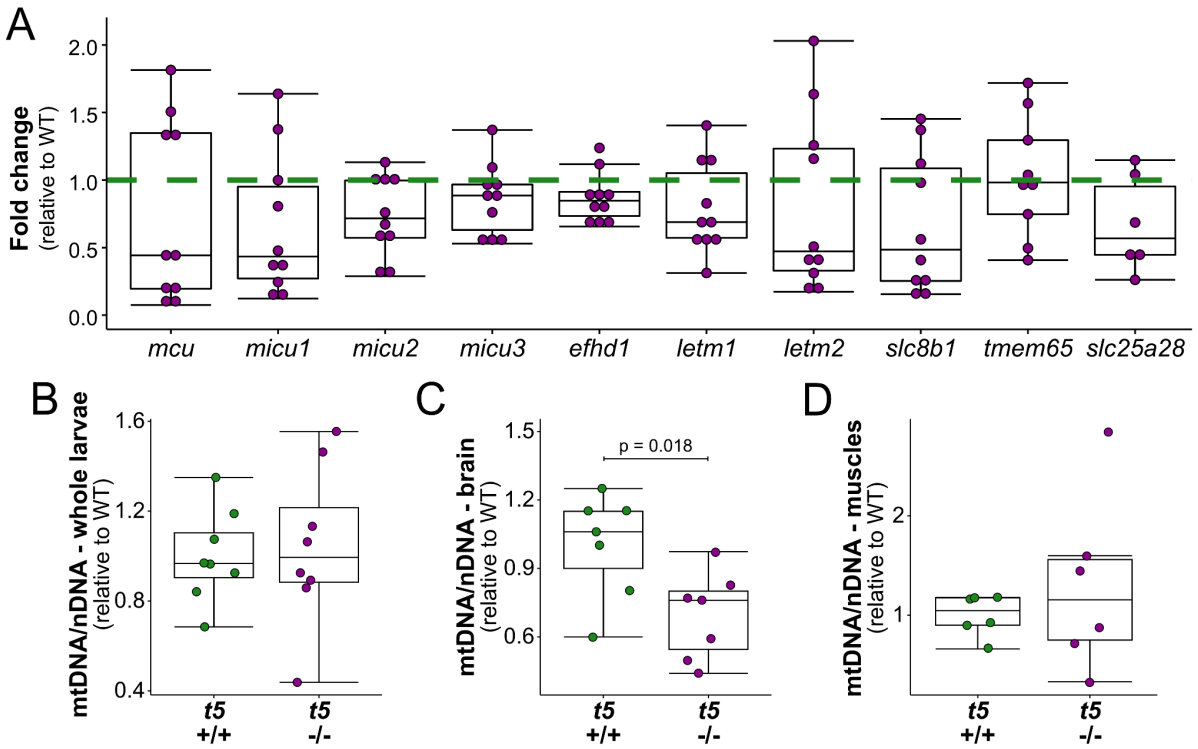

Figure EV4. Tmbim5 deficiency does not affect expression of genes encoding mitochondrial proteins involved in Ca^{2+} transport in zebrafish larvae

A) mRNA levels of proteins involved in mitochondrial Ca^{2+} transport were quantified by qPCR in 5 dpf *tmbim5*$^{-/-}$ larvae and normalized to WT. *rpl13a* and *ef1a* were used as reference genes. Results are presented as box-and-whisker plots (box: 25th–75th percentile; whiskers: min to max), with each dot representing an independent biological replicate (n = 6–10, with each RNA sample isolated from 30 larvae). Number of experiments = 5. Statistical analysis: one-sample *t*-test with BH correction for multiple comparisons.

B–D) The mitochondrial (mtDNA) to nuclear DNA (nDNA) ratio is decreased in the brain of *tmbim5*$^{-/-}$ zebrafish but remains unchanged in muscles and 5 dpf *tmbim5*$^{-/-}$ larvae. The mtDNA/nDNA ratio was quantified by qPCR and normalized to WT. *mt-nd1* (*mitochondrial NADH dehydrogenase 1*) was used as a marker for mtDNA, while *ef1a* was used for nDNA. B) mtDNA/nDNA ratio in 5 dpf larvae. n = 8 (each DNA sample was isolated from 30 larvae). Number of experiments = 3. Statistical analysis: *t*-test. C–D) mtDNA/nDNA ratio in the brains (C) and muscles (D) of adult (1.5-year-old) zebrafish. n = 6 (each DNA sample was isolated from one fish). Number of experiments = 2. Statistical analysis: *t*-test (brain) or Mann–Whitney test (muscles).

Na^+-dependent Ca^{2+} efflux remained unchanged after CGP treatment

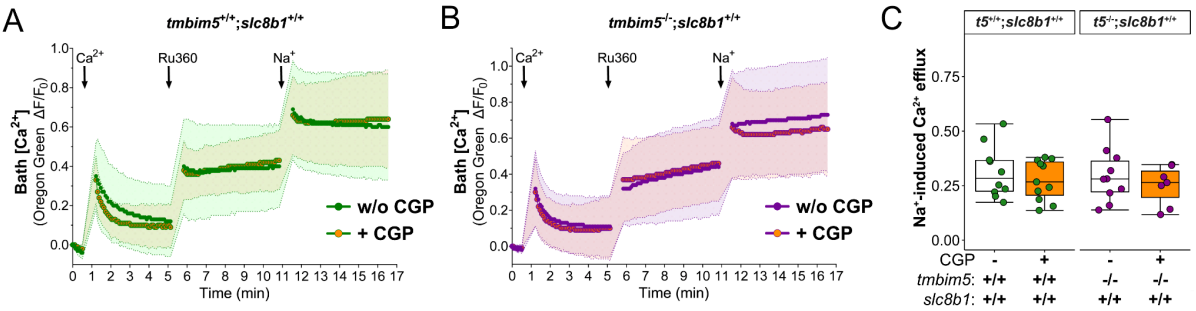

Figure EV5. Na^+-dependent Ca^{2+} efflux remained unchanged after CGP treatment.

A–B) Changes in bath Ca^{2+} levels measured by Oregon Green 488 BAPTA-5N under basal conditions and after treatment with CGP-37157 (10 μM) in mitochondria isolated from: (A) *tmbim5*$^{+/+}$ and (B) *tmbim5*$^{-/-}$. Mitochondria were first loaded with Ca^{2+} (20 μM), and Ru360 (10 μM) was added to inhibit Ca^{2+} influx. Subsequently, Na^+ (10 mM) was added to measure Ca^{2+} efflux via NCLX. Fluorescence of Oregon Green 488 BAPTA-5N was normalized to the initial value (F_0). Data are presented as mean ± SD $\Delta F/F_0$ traces.

C) Ca^{2+} efflux from mitochondria after Na^+ addition remained unchanged following CGP treatment. To quantify Ca^{2+} efflux, the last $\Delta F/F_0$ value recorded after Ru360 addition was subtracted from the maximal $\Delta F/F_0$ observed after Na^+ addition. Results are presented as box-and-whisker plots (box: 25th–75th percentile; whiskers: min to max), with each dot representing an independent biological replicate (n = 7–12). Statistical analysis: *t*-test or Mann–Whitney test.

Generation of Slc8b1-deficient fish

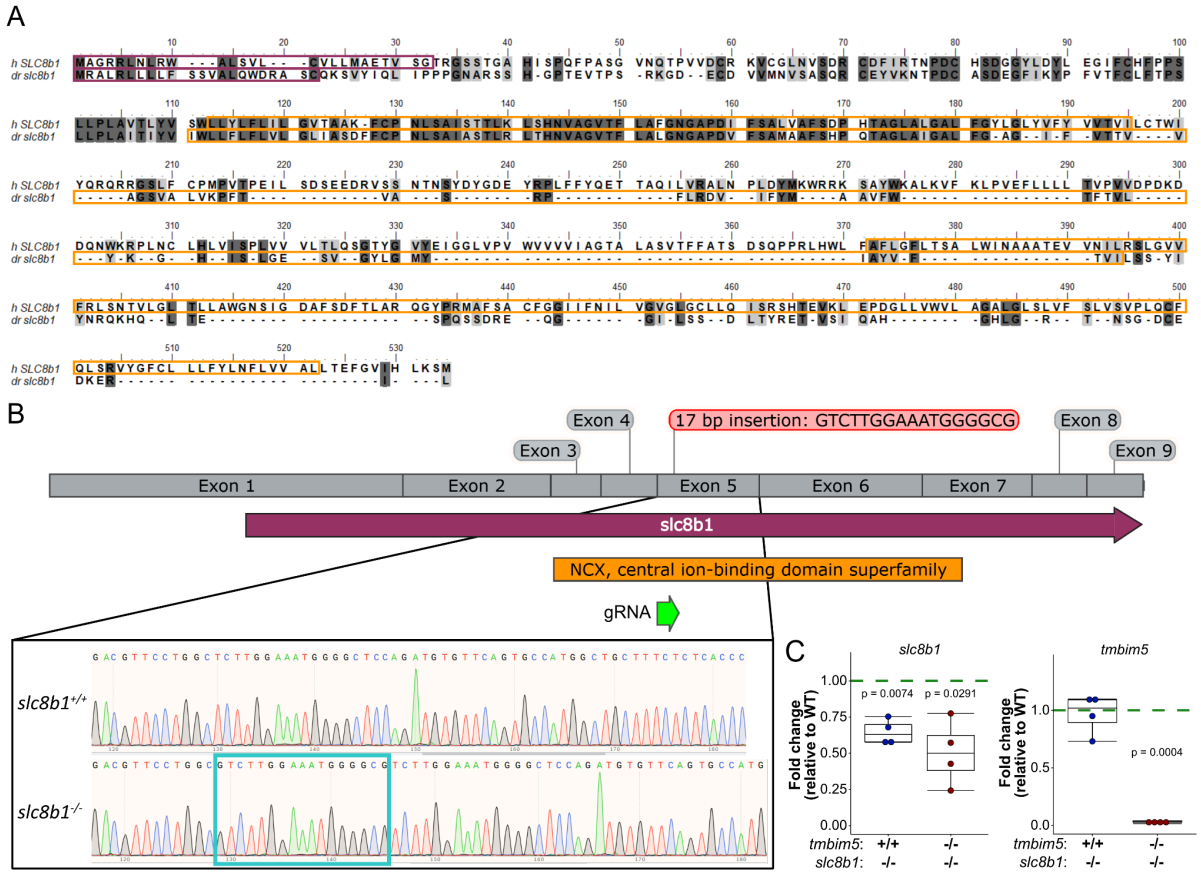

Figure EV6. Generation of Slc8b1-deficient fish

A) Sequence alignment of human and zebrafish NCLX proteins encoded by *slc8b1*, performed using Optimal Global Alignment with the BLOSUM62 similarity matrix. The alignment revealed 24% sequence identity between species. Identical residues are highlighted in dark gray, while residues with similar physico-chemical properties are marked in light gray. The predicted signal peptide is enclosed within a violet frame, and the sodium/calcium (Na^+/Ca^{2+}) domain is highlighted by an orange frame.

B) Schematic representation of the mutation site in *slc8b1*, accompanied by Sanger sequencing results. Inserted base pairs are highlighted with a turquoise frame.

C) Expression levels of *slc8b1* and *tmbim5* mRNA in 5 dpf *tmbim5*$^{+/+}$;*slc8b1*$^{-/-}$ and *tmbim5*$^{-/-}$;*slc8b1*$^{-/-}$ larvae, quantified using qPCR and normalized to wild-type. *rpl13a* and *ef1a* were used as reference genes. Results are presented as box-and-whisker plots (box: 25th–75th percentile, whiskers: min–max), with each dot representing an independent biological replicate (n = 4, each RNA sample isolated from 30 larvae). Statistical analysis: one-sample t-test with BH correction for multiple comparisons.